Geomorphology 295 (2017) 337–353

Contents lists available at ScienceDirect

Geomorphology

journal homepage: www.elsevier.com/locate/geomorph

Transient Quaternary erosion and tectonic inversion of the Northern Range, Trinidad

Jeanette C. Arkle[a,*], Lewis A. Owen[a], John Weber[b], Marc W. Caffee[c,d], Sarah Hammer[a]

[a] Department of Geology, University of Cincinnati, Cincinnati, OH 45221, USA
[b] Department of Geology, Grand Valley State University, 1 Campus Drive, Allendale, MI 49401, USA
[c] Department of Physics and Astronomy/PRIME Laboratory, Purdue University, West Lafayette, IN 47907, USA
[d] Department of Earth, Atmospheric, and Planetary Sciences, Purdue University, West Lafayette, IN 47907, USA

ARTICLE INFO

Keywords:
Cosmogenic nuclide
Thermochronology
Geomorphology
Caribbean

ABSTRACT

Cosmogenic ^{10}Be measured in sediments from Northern Range catchments on the island of Trinidad reveals low millennial-scale rates of erosion (average ~40 mm/ka) that increase roughly eightfold, from 11 to 92 mm/ka, eastward across the mountain range. These results, in conjunction with an analysis of mountain morphometrics, are consistent with Quaternary east-side-up tilting of the Northern Range, which has occurred recently (~100 ka). The highest millennial-scale erosion rates coincide spatially with Quaternary east-side surface uplift (albeit not in magnitude), high modern rainfall rates, low topographic relief, and convex longitudinal stream profiles, indicating transient Quaternary erosion. We interpret that hillslope adjustment and erosion of the Northern Range is buffered from climatic and tectonic forcings by dense tropical vegetation cover, thick saprolite, and porous regolith. Compared with longer-term, thermochronology exhumation rates, we document that an order of magnitude deceleration of and reversal in the locus of erosion and exhumation has occurred during the Pliocene to the Holocene. We suggest that these combined data sets highlight distinct syn- and post-collisional phases of Northern Range development that are related to a major change in relative Caribbean-South American plate motion from oblique convergence to transform motion. Oblique collision during the mid-Miocene likely caused relatively higher rates of and asymmetric exhumation of the Northern Range. Post-collisional mountain-scale tilting is likely caused by a combination of crustal extension in the Gulf of Paria and by deep subsurface lithospheric detachment processes that drives dynamic topography.

1. Introduction

Erosion of post-collisional mountain belts is expected to decay through time as the production of topographic relief is reduced. Yet deviations from this progressive deceleration of erosional efflux in post-collisional mountain belts can occur from various internal and external variables, such as post-orogenic tectonism, climate fluctuations, fluvial adjustments, base-level changes, and geodynamic aberrations (Kooi and Beaumont, 1996; Pazzaglia and Brandon, 1996; Reiners et al., 2003; Allen, 2008). These and other post-collisional dynamics may be recorded by temporal variations in erosion rates, which can be quantified with techniques such as cosmogenic ^{10}Be methods and low-temperature thermochronology (Granger et al., 1996; Reiners et al., 2003). Previous studies have used temporal and spatial patterns of erosion to reconstruct the distribution and rates of faulting (Cyr et al., 2010; Gudmundsdottir et al., 2013), to assess the steadiness or transience of landscapes (Small and Anderson, 1998; Willett and Brandon, 2002), and to identify the relative importance of tectonic and environmental factors in controlling mountain landscape evolution (Riebe et al., 2003; von Blanckenburg et al., 2004; Portenga and Bierman, 2011; Acosta et al., 2015). In this study, we examine temporal and spatial variations in erosion rates during the syn- and post-collisional phases of the Northern Range, a mountain range on the island of Trinidad, which is located in the southeastern Caribbean-South American plate boundary zone (Fig. 1).

The Northern Range in Trinidad is the easternmost extent of a long, narrow metamorphic hinterland along the north coast of South America that is in a post-collisional phase of development (Fig. 1). The late Tertiary evolution of the Northern Range has progressed through a major tectonic change from relative Caribbean-South American oblique-collision to transform motion during the late Miocene (Pindell et al., 1998; Babb and Mann, 1999). Thermochronology studies in the Northern Range and nearby in the Central Range indicate that the main phase of mountain building in Trinidad — in the geodynamic sense of

* Corresponding author.
E-mail address: arklejc@mail.uc.edu (J.C. Arkle).

http://dx.doi.org/10.1016/j.geomorph.2017.07.013
Received 10 February 2017; Received in revised form 14 July 2017; Accepted 14 July 2017
Available online 20 July 2017
0169-555X/

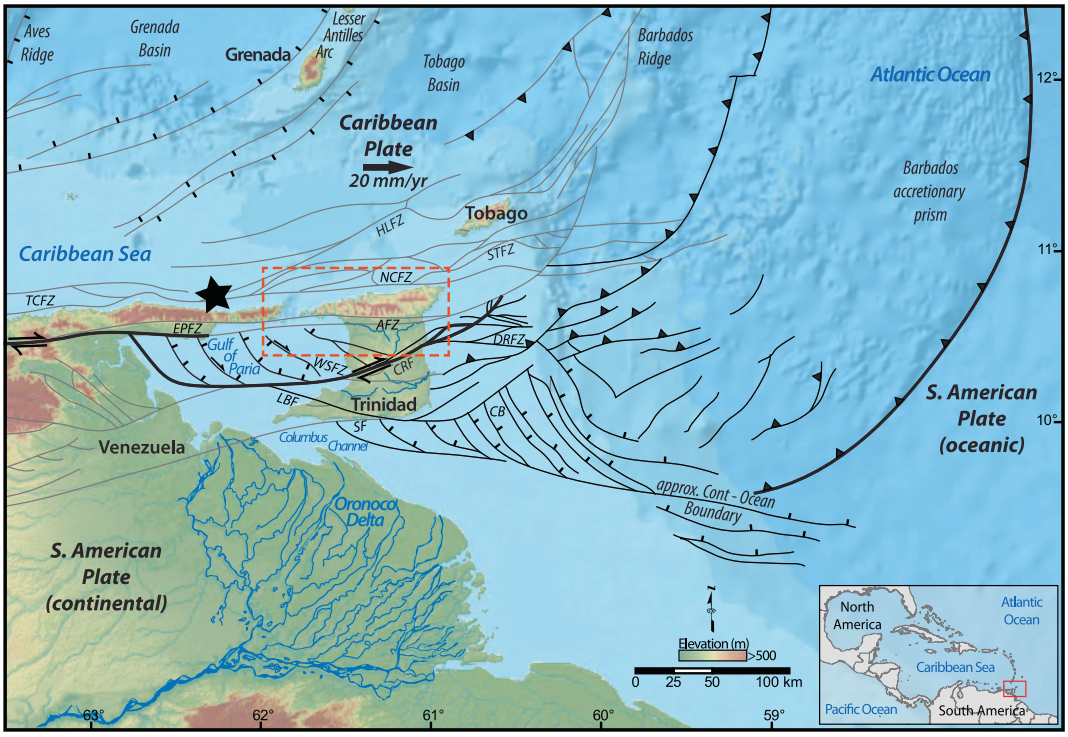

Fig. 1. Overview of the southeast Caribbean showing topography (0.5 km DEM from the U.S. Geological Survey), bathymetry (from ESRI base maps), and major (bold black lines) and minor faults (thin grey lines) showing relative motion where known — thrust (teeth), normal (bar), and strike-slip (arrows) (after Prentice et al., 2010; Soto et al., 2011; Garciacaro et al., 2011). Relative Caribbean-South American plate vector is from Weber et al. (2001a, 2011). Black star marks the approximate location of the *Paria Cluster* of seismicity (Russo and Speed, 1992). The dashed red box outlines the Northern Range study area, also shown in Figs. 2 and 3. TCFZ – Tortuga Coche Fault zone; EPFZ – El Pilar Fault zone; AFZ – Arima Fault zone; CRF – Central Range Fault; WSFZ – Warm Springs Fault zone; LBF – Los Bajos Fault; SF – Soldado Fault; DRFZ –Darien Ridge Fault zone; CB – Columbus Basin; NCFZ – North Coast Fault zone; STFZ – Southern Tobago Fault zone; HLFZ – Hinge Line Fault zone. (For interpretation of the references to color in this figure legend, the reader is referred to the web version of this article.)

active shortening, crustal thickening, and rock exhumation — occurred primarily during the Miocene and Pliocene (Algar et al., 1998; Weber et al., 2001b; Giorgis et al., 2016). Miocene oblique collision focused crustal thickening, uplift, and exhumation in the metamorphic hinterland, i.e., in the Northern Range, resulting in the exposure of mid- to upper-crustal rocks that decrease in metamorphic grade and contain less ductile structures and fabrics eastward (Frey et al., 1988; Foland et al., 1992; Algar and Pindell, 1993; Algar et al., 1998; Weber et al., 2001b). Subsequently, at ~10 Ma, the Caribbean-South American plate boundary stepped southward and changed to its current phase of transform plate motion, which is now focused along the Central Range Fault, some 30 km south of the Northern Range (Algar and Pindell, 1993; Pindell et al., 1998; Babb and Mann, 1999; Weber et al., 2001a). Although this change in relative plate motion likely had a profound effect on structural reorganization and on the distribution of tectonism in Trinidad, it is unclear whether or to what extent it has impacted the Quaternary evolution of the Northern Range. Geomorphic patterns and estimates of surface uplift rates from Quaternary marine terraces, however, have led to the hypothesis of range-wide, post-collisional, east-side-up tilting of the Northern Range (Weber, 2005; Ritter and Weber, 2007). Deep and diffuse seismicity does exist under the Northern Range despite the fact that geodetic studies indicate modern plate motion is focused on a largely aseismic creeping or locked Central Range Fault (Weber et al., 2001a, 2011; Churches et al., 2014). Tectonics in this region are further influenced by the transition from westward subduction of the oceanic South American plate to strike-slip motion between continental South America and the Caribbean plate (e.g., Molnar and Sykes, 1969; Russo and Speed, 1992; Levander et al., 2014). Constraints on the post-collisional evolution of the Northern Range have important implications for understanding the regional neotectonics, plate tectonic history, and landscape dynamics in this region.

In this study, we characterize the geomorphology and quantify erosion rates using cosmogenic ^{10}Be analysis on sediment samples from 26 catchments in the Northern Range (Fig. 2). Our objectives were to (i) evaluate temporal variations of erosion during the syn- and post-collisional phases of the Northern Range by comparing our millennial-scale (10^3–10^4 years) cosmogenic nuclide data with preexisting long-term (10^6 years) exhumation rate data from thermochronometers; (ii) characterize the Quaternary landscape evolution of the Northern Range, specifically investigating the hypothesis of late-stage, east-side-up tectonic tilting; and (iii) investigate the steadiness or transience of Northern Range topography during the Quaternary by comparing millennial-scale erosion rates to surface uplift rates derived from marine terraces and by exploring the relationships between surface processes, tectonics, and climate on millennial timescales.

2. Regional setting

2.1. Geologic setting

The Northern Range is located in the northeast corner of continental South America and north of the current Caribbean and South American transform plate boundary, the Central Range Fault, in Trinidad (Fig. 1). The Caribbean-South American transform plate boundary strikes E-W along northern Venezuela, steps right in the Gulf of Paria, and then strikes ~N72E through central Trinidad as the Central Range Fault (Babb and Mann, 1999; Weber et al., 2001a, 2011). The current relative Caribbean plate velocity is ~20 mm/a toward ~N86°E in Trinidad (Weber et al., 2001a, 2011). The majority of current Caribbean plate boundary dextral shear, ~12–15 mm/a, is accommodated along the Central Range Fault in central Trinidad (Weber et al., 2001a, 2011).

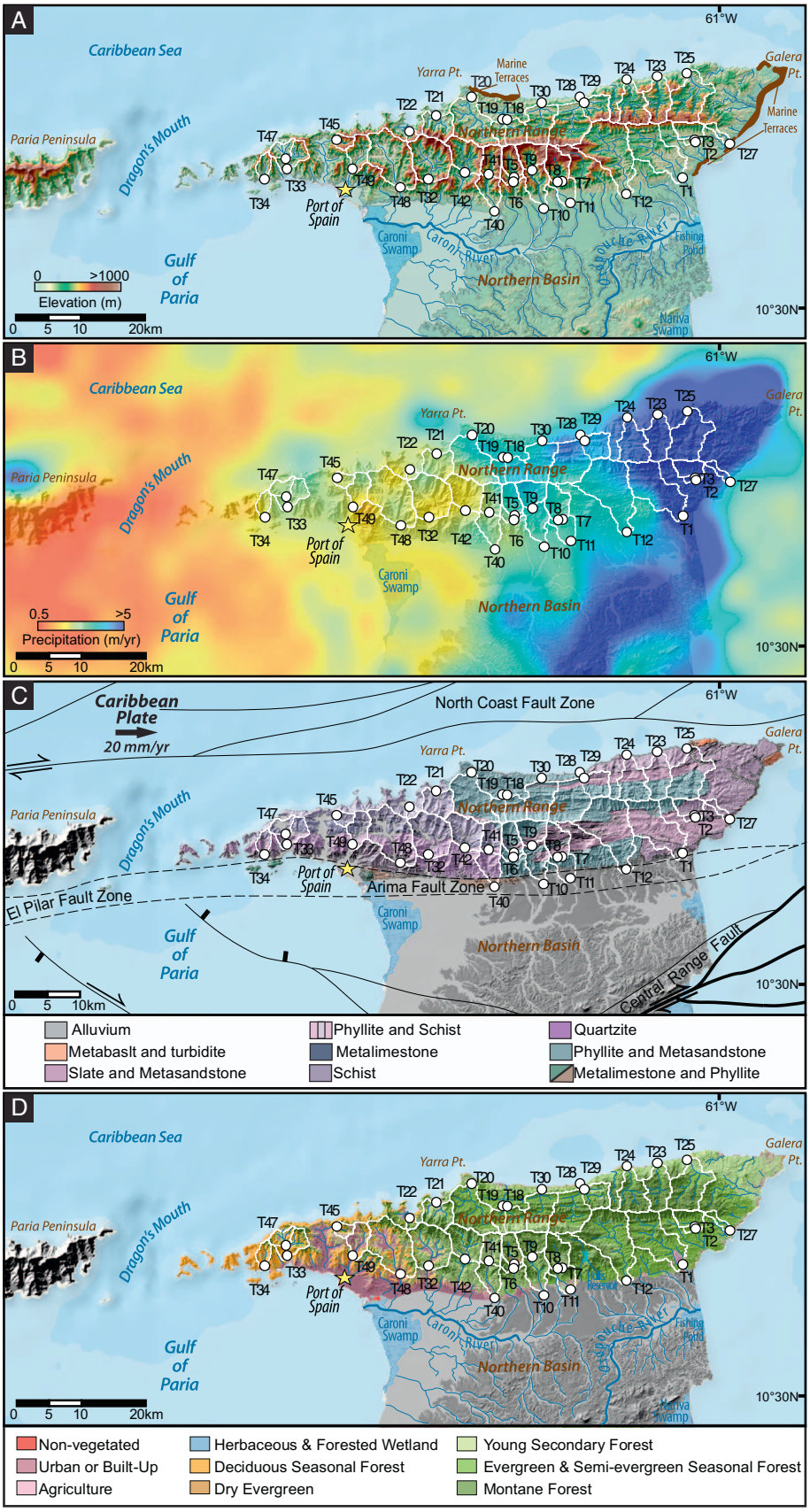

Fig. 2. Catchments (white outlines) and ^{10}Be sample locations studied in the Northern Range of Trinidad. (A) Topography of the Northern Range showing major landforms, rivers, and wetlands. (B) Precipitation rates over the region averaged as mean annual precipitation over 12 years (1998–2009) from Bookhagen (2013). (C) Simplified geology showing major faults and relative plate motion vector (modified from Weber et al., 2001a, 2011; de Verteuil et al., 2006; Prentice et al., 2010; Soto et al., 2011). (D) Vegetation and land cover data from Helmer et al. (2012). For simplicity, lithology and vegetation (C, D) are shown only in the Northern Range.

Dextral plate motion occurs between the oceanic Caribbean and continental South American plates (i.e., covered Guyana Shield), and west-directed subduction of the oceanic South American plate occurs beneath the Caribbean plate (Speed et al., 1991; Algar and Pindell, 1993; Russo and Speed, 1994; Pindell et al., 1998; Soto et al., 2011). To the west of Trinidad and in offshore northern Venezuela, the *Paria*

Cluster of seismicity (star in Fig. 1) is interpreted to mark the location of lithospheric detachment, which facilitates the deep, subsurface transition from subduction to transform plate motion (Molnar and Sykes, 1969; Russo and Speed, 1992; Levander et al., 2014).

The Northern Range rises to 940 m above mean sea level (amsl) and is a thick and buoyant metamorphic hinterland welt that formed between the Caribbean and South American plates (Speed et al., 1991; Pindell et al., 1998). Mid-Miocene oblique collision led to metamorphism and exhumation of this narrow, east-trending belt of Jurassic-Cretaceous sedimentary protolith rocks, which have mid-Miocene metamorphic ages (Foland et al., 1992; Weber et al., 2001b). These rocks form a nearly continuous mountain belt from the Cordillera de la Costa in Venezuela to the Northern Range in Trinidad (Frey et al., 1988; Foland et al., 1992; Algar et al., 1998). Apatite and zircon fission-track ages from the Northern Range and eastern Paria Peninsula indicate that rocks were exhumed from depths of ~10 km from ~36 to 4 Ma (Algar et al., 1998; Weber et al., 2001b; Cruz et al., 2007; Denison, 2008). Rocks with higher metamorphic grades and younger fission-track ages in the western Northern Range and eastern Paria Peninsula indicate asymmetric exhumation occurring into the Pliocene, with exhumation decreasing eastward (Frey et al., 1988; Algar et al., 1998; Weber et al., 2001b; Denison, 2008).

The Northern Range is bound to the north by the North Coast Fault zone and to the south by the Northern Basin and the Arima Fault, which is the on-strike extension of the active El Pilar Fault in Venezuela (Figs. 1, 2). These faults could have accommodated some Quaternary motion, but geodesy and geologic evidence indicate that these structures are tectonically dead (Algar and Pindell, 1993; Weber et al., 2001b). Quaternary sedimentary deposits in the Northern Basin are in contact with the deeply exhumed Mesozoic metamorphosed Northern Range bedrock across the Arima Fault. This contact generates a sharp transition and creates a somewhat faceted mountain front. However, no historic nor fossil motion has been identified along the Arima Fault, indicating it is likely an exhumed fault line scarp that marks a *line* of differential erosion along the range front (Algar and Pindell, 1993; Weber et al., 2001b).

2.2. Geomorphic setting

Northern Range topography transitions from low-elevation, high-relief topography in the west to elevated, low-relief topography in the east. Weber (2005) and Ritter and Weber (2007) reasoned that an eastward transition from subsidence to uplift largely controls these and additional (see below) topographic transitions in the Northern Range, and they defined an ~N-S axis of tilt that occurs roughly at Yarra Point (Fig. 2). In this paper, we follow this earlier work and use the term tectonic tilting to describe differential vertical tectonic movement normal to this tilt axis, which Ritter and Weber (2007) argued separates a submergent landscape to the west from an eastern emergent landscape. In the west, topography is extremely dissected, the coast is scalloped, and drainage divides of the westernmost catchments are at or near sea level. Drainage capture of what were likely once catchment divides has formed isolated islands in the Dragon's Mouth Passage that separates Trinidad from Venezuela (Figs. 2, 3). The eastern Northern Range, in contrast, contains marine terraces exposed at elevations ranging from ~5 to 45 m amsl (Figs. 2, 3; Kugler, 1959). The terraces are cut into metamorphic bedrock and capped by unconsolidated quartz-rich Quaternary sediments (Kugler, 1959). Along the northeast coast, quartz from marine terrace sediments located at elevations of ~13 and 21 m amsl yield optically stimulated luminescence ages of ~40 ± 3 and 74 ± 5 ka, respectively (Morell, 2009). In addition, mountain front sinuosity decreases eastward along the southern range front, and incised Quaternary alluvial fans are present only along the eastern flank of the range. Similar range-front alluvial fans have subsided to depths over ~100 m in the west and are concealed under the Caroni Swamp (Weber, 2005; Ritter and Weber, 2007).

Fluvial networks draining the Northern Range are mostly transport-limited systems, consisting of large boulder and clay to cobble cover. Fluvial channels are incised into hillslopes that are mantled with thick (> 2 m) saprolite and soil. Stream channels on the east side of the range are V-shaped, and some have steep (> 45°) narrow (< 1 m) channels. Streams in western catchments have formed relatively flat, broad (> 1 km) valley floors, and alluvial fill covers the basement with sediment thicknesses to ~110 m (Weber, 2005; Ritter and Weber, 2007). Eastward across the range, stream outlet elevations increase from near sea level up to ~138 m amsl along the southern mountain front (Ritter and Weber, 2007).

2.3. Climate, vegetation, and modern land use

Trinidad is located at a latitude of ~10°N and has a tropical maritime climate with wet (June–December) and dry (January–May) seasons and relatively high average annual temperatures (~25 °C) and humidity (~70%; WRA, 2001). Trinidad experiences strong easterly trade winds and tropical storms, but it is located outside of the main Atlantic hurricane belt. Hurricanes do, however, occasionally track across the island; the most recent ones occurred in 1963 and 1993. The convergence of the northeast trade winds from the Atlantic with the Northern Range causes a steep precipitation gradient along the mountains, with annual rainfall decreasing westward from ~5 to 0.3 m/a (Fig. 2; Bookhagen, 2013). Precipitation is generally symmetric across the mountain divide, with the annual rainfall over the high peaks ranging from ~2–5 m/a and is ~0.3–3 m/a along the southern flank and north coast.

The strong east-west rainfall gradient influences vegetation cover and type in the Northern Range, which also varies with elevation, hillslope aspect, and soil type (Beard, 1946; Helmer et al., 2012). Native vegetation assemblages transition from evergreen seasonal and montane forests in the east and at high elevations (> 700 m amsl), to semideciduous and deciduous forests westward. Semidry evergreen forests and woodlands occur at lower and coastal elevations (Fig. 2; Beard, 1946; Helmer et al., 2012). Endemic vegetation in Trinidad has been modified since the sixteenth century, with primary vegetation replaced in some areas by pasture or agriculture including coconut, sugarcane, pine forest (logging), bamboo, and tobacco (Helmer et al., 2012). Urbanization, forest fires, and rock quarrying have also altered the natural vegetation and modified the landscape.

Marine paleoclimate records from the nearby Cariaco Basin in Venezuela show that late Quaternary climatic shifts in the region are generally consistent with global stadials and interstadials (Peterson et al., 2000; Haug et al., 2001). Temperature records show that it may have been ~5 °C cooler than present in tropical low-latitude areas of South America during glacial stadials (van der Hammen and Hooghiemstra, 2000). No evidence has been found for Pleistocene glaciation in the Northern Range, although the Venezuelan Andes, which are several thousand meters higher but at similar latitudes and to the west, were glaciated (e.g., Wesnousky et al., 2012). Climatic transitions into cooler and more arid periods likely caused vegetation changes from wet forests to dry forests and to arid grasslands and savanna and caused upslope shifts of montane vegetation (van der Hammen and Hooghiemstra, 2000; Hughen et al., 2004).

Differential vertical tectonism across the region makes it extremely difficult to determine the absolute magnitudes of local sea-level change. If consistent with eustatic sea-level changes, the Caribbean Sea may have been ~120 m lower than present during the global last glacial maximum (e.g., Peltier and Fairbanks, 2006). Positioned aside the shallow (< 30 m depth) Gulf of Paria, Trinidad was likely connected to South America during the early part of the Holocene. Extensive regions of the shallow northern continental shelf that are presently at depths of < 100 m may have also connected Trinidad with Tobago during the Pleistocene.

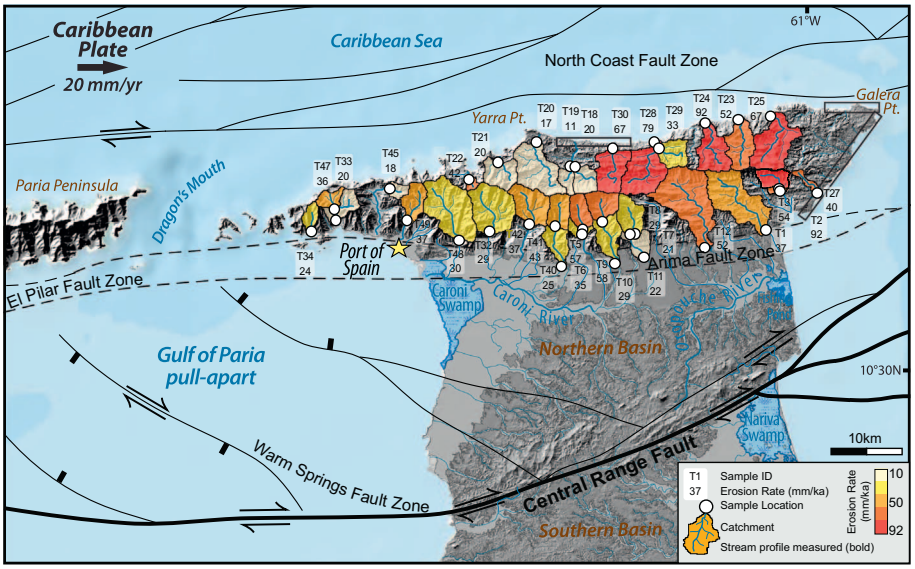

Fig. 3. Erosion rates for catchments in the Northern Range of Trinidad plotted on a 30 m DEM showing major faults (black lines), cosmogenic ^{10}Be sample locations (white dots), catchments (outlined by black) colored according to corresponding erosion rates, swaths where marine terraces are located along the north and northeast coasts (black rectangles), and locations of measured longitudinal stream profiles (bold blue lines) shown in Figs. 5 and S2. Major faults and relative plate motion vector are from Weber et al. (2001a, 2011), de Verteuil et al. (2006), Prentice et al. (2010), Soto et al. (2011). (For interpretation of the references to color in this figure legend, the reader is referred to the web version of this article.)

3. Methods

3.1. Cosmogenic ^{10}Be methods

Catchment-wide erosion rates from the Northern Range were determined using cosmogenic ^{10}Be methods from quartz collected from stream sediment (Figs. 3, S1). The ^{10}Be that is produced in quartz in rock and regolith in the uppermost ~3 m of Earth's surface is formed via spallation reactions with cosmic rays; the reactions decrease exponentially with depth in the substrate (Lal, 1991). The average erosion rate is inversely proportional to the surface ^{10}Be concentration and is integrated over the time required to erode one cosmic ray penetration length (1 e-folding depth), ~100 and ~60 cm for regolith and bedrock respectively (equations in Lal, 1991; Granger et al., 1996). Catchment-averaged ^{10}Be erosion rates are a measure of physical and chemical denudation and typically reflect erosional processes over ~10^3 to 10^5 year timescales (Bierman and Steig, 1996; von Blanckenburg et al., 2004).

3.2. Sampling

Sediment samples were collected from nearly every major stream that drains the Northern Range: 33 samples in total from 26 catchments (Fig. 3; Table 1). We collected multiple samples in seven catchments: at least one sample from the stream mouth and 1–2 samples upstream, either immediately below (n = 2) or above (n = 5) major knickpoints expressed in the landscape as waterfalls. Most stream mouth samples were collected > 10 m downstream of inner-catchment tributaries to minimize the effects of large landslides and to ensure complete sediment mixing (Niemi et al., 2005; Yanites et al., 2009). Samples were collected from sediment in active stream channels (Fig. S1). From streams that drain directly into the Caribbean Sea or Atlantic Ocean, sediment samples were collected upstream of the confluence above high/storm-tide levels to avoid contamination by beach sand. We avoided channel sediment from areas potentially influenced by local streambank slumps, landslides, and anthropogenic inputs.

3.3. Laboratory methods for cosmogenic ^{10}Be

We extracted quartz, and ultimately Be, from samples by standard methods of HF dissolution and column chromatography following Kohl and Nishiizumi (1992) and detailed below. More than 2 kg of sediment, < 2 cm in diameter, was collected and then crushed and sieved to obtain a 250–500 μm particle size fraction. This crushed fraction was put through a Franz magnetic separator to help remove magnetic minerals and feldspars. The nonmagnetic fractions were chemically leached using aqua regia acid for > 12 h, and one or more 5% HF/HNO_3 leaches for ~24 h. Remaining nonquartz minerals were removed using heavy liquid (lithium heteropolytungstate) separation. The purity of the quartz separate was examined using an optical microscope or tested with infrared stimulated luminescence in a Risø optically stimulated luminescence reader. The quartz was then leached in 1% HF/HNO_3. The pure quartz was spiked with a ^{9}Be carrier and dissolved in 48–50% HF, following which the solution was taken to dryness in a fume hood. The samples were fumed three times with $HClO_4$. The residue was then passed through anion and cation exchange columns to separate the Be fraction. Ammonium hydroxide was added to the Be fractions to precipitate $Be(OH)_2$ gel. The gel was rinsed and dried in acid-cleaned quartz crucibles for ~24 h. Once dry, the samples were calcinated to BeO by ignition at 750 °C for 5 min. The BeO was mixed with Nb powder and loaded into steel targets. The ^{10}Be concentrations were determined from ^{10}Be/^{9}Be ratios measured by accelerator mass spectrometry at PRIME Laboratory at Purdue University with the 07KNSTD standard and ^{10}Be half-life of 1.36 Ma (Nishiizumi et al., 2007).

3.4. Cosmogenic ^{10}Be production rates and erosion rates

Cosmogenic production rates of ^{10}Be were determined for each pixel in a catchment from a 1-arc-second (30 m) resolution DEM. We used the Borchers et al. (2016) production rate of 4.01 ^{10}Be atoms/g SiO_2/a with the Lal (1991) and Stone (2000) time independent scaling framework and accounted for production of fast and slow muon and neutron attenuation (Stone, 2000) for each pixel. Corrections for topographic shielding were determined from the maximum angle to the horizon for each pixel probing at 10° azimuth increments following methods of Dortch et al., 2011 using MATLAB (v. 2009). Erosion rates were calculated with the catchment-averaged production rates using equations (Lal, 1991; Granger et al., 1996) and numerical functions from the CRONUS calculator (Balco et al., 2008). Associated 1σ uncertainty was propagated through the erosion rate calculations (Table 2).

Portenga et al. (2015) highlighted the importance of measuring native ^{9}Be in quartz when calculating erosion rates based on cosmogenic ^{10}Be as some quartz samples contained significant native ^{9}Be. Most previous studies have assumed that the amount of native ^{9}Be in quartz is much less than the amount added by the ^{9}Be carrier so that native ^{9}Be can be ignored. In some instances, however, particularly

Table 1
Sample locations and catchment metrics.

Sample	Stream name	Lat.	Long.	Stream sample	Catchment area	Elevation range & mean			Relief	Slope mean	HI	Precip.	Lithology	Vegetation cover	Land modification	Stream gradient	Distance from tilt axis
		(°N)[a]	(°W)[a]	Location	(km^2)	(m)[b]			(m)[c]	(°)[d]	(Elev./ relief)[e]	(m/yr)[f]	(% area)[g]	(% area)[g]	(% area)[g]	(m/km)[h]	(km)[i]
T1	Matura	10.68	61.05	Mouth	46	7–595		(166)	588	14	0.27	3.1	35	100	6	14	27
T2	Arroyo Seco	10.73	61.04	Upstream	11	74–525		(214)	451	17	0.31	3.7	97	100	0	63	33
T3	Arroyo Seco	10.73	61.03	Mouth	13	45–525		(202)	480	17	0.33	3.7	95	100	0	60	33
T5	Arima	10.68	61.29	Upstream	12	162–820		(402)	658	20	0.37	2.0	85	97	40	34	5
T6	Arima	10.68	61.29	Mouth	16	155–820		(393)	665	21	0.36	2.0	88	98	35	29	5
T7	Aripo	10.68	61.22	Upstream	17	140–916		(456)	776	18	0.41	2.0	24	100	27	50	12
T8	Aripo	10.68	61.22	Upstream	17	148–916		(456)	768	18	0.40	2.0	24	100	27	50	12
T9	Guanapo	10.69	61.26	Upstream	16	134–916		(451)	782	20	0.41	2.3	64	100	23	31	8
T10	Guanapo	10.64	61.25	Mouth	33	49–916		(345)	866	19	0.34	2.2	64	98	34	18	8
T11	Aripo	10.65	61.21	Mouth	28	45–916		(338)	871	15	0.34	2.0	34	98	33	36	12
T12	Oropuche	10.66	61.13	Mouth	58	37–745		(235)	708	17	0.28	2.3	52	100	11	12	20
T18	Marianne	10.77	61.30	Upstream	6	45–722		(201)	677	18	0.23	2.3	100	99	11	24	5
T19	Marianne	10.77	61.30	Upstream	20	29–828		(230)	799	20	0.25	2.3	94	100	19	28	4
T20	Yarra	10.80	61.35	Mouth	36	6–697		(158)	691	18	0.22	1.9	93	100	5	8	−0.1
T21	Curaguate	10.77	61.40	Mouth	18	9–851		(191)	842	21	0.22	1.6	100	100	37	37	−5
T22	N. Maracus	10.75	61.44	Upstream	2	9–678		(271)	669	27	0.39	1.7	100	100	9	37	−10
T23	Shark	10.82	61.09	Mouth	22	4–593		(287)	589	16	0.48	3.4	70	100	8	35	29
T24	Matelot	10.82	61.13	Mouth	23	2–632		(295)	630	19	0.47	2.9	74	100	8	46	25
T25	Grande	10.83	61.05	Mouth	35	3–561		(249)	558	16	0.44	4.5	82	100	18	37	33
T27	Sena	10.73	60.99	Mouth	4	2–399		(145)	397	13	0.36	3.1	83	98	18	26	37
T28	Madamas	10.80	61.19	Mouth	47	9–923		(246)	914	19	0.26	2.4	84	100	12	31	16
T29	Madamas	10.79	61.19	Upstream	14	28–645		(236)	617	18	0.34	2.5	70	100	20	33	16
T30	Paria	10.79	61.25	Mouth	24	6–924		(232)	918	18	0.25	2.4	86	100	21	24	10
T32	S. Maracus	10.68	61.41	Mouth	37	56–915		(298)	859	22	0.28	1.4	93	94	52	27	−7
T33	Cuera	10.70	61.61	Mouth	20	5–533		(155)	528	17	0.29	1.7	61	98	28	5	−29
T34	Chaguaramas	10.68	61.64	Mouth	7	2–538		(202)	536	22	0.37	1.4	86	95	23	30	−33
T40	Arouca	10.64	61.32	Mouth	28	39–711		(314)	673	21	0.41	1.7	92	97	60	19	1
T41	Arouca	10.69	61.32	Upstream	14	164–711		(381)	547	21	0.40	1.7	87	98	62	22	2
T42	Caura	10.69	61.36	Mouth	24	88–827		(301)	739	20	0.29	1.4	86	100	29	25	−2
T45	Diego Martin	10.74	61.54	Upstream	5	71–668		(340)	597	19	0.45	1.5	58	98	45	26	−20
T47	Tucker	10.71	61.61	Upstream	8	20–533		(130)	513	14	0.22	1.6	61	96	38	2	−30
T48	Santa Cruz	10.67	61.45	Mouth	47	35–715		(224)	680	20	0.28	1.4	78	89	42	8	−13
T49	Maraval	10.70	61.52	Upstream	14	31–669		(244)	637	20	0.33	1.4	61	80	64	33	−18
				Average:	22	50	724	273	673	19	0.33	2.2	75	98	26	29	6
				Maximum:	58	164	924	457	918	27	0.48	4.5	100	100	64	63	37
				Minimum:	2	2	399	130	397	13	0.22	1.4	24	80	0	2	0.1

[a] Latitude and longitude coordinate datum are reported in WGS 84, zone 20P.
[b] Elevation is the minimum - maximum and mean (brackets) elevation of a catchment.
[c] Relief is the difference between the maximum and minimum elevation in a catchment.
[d] Slope is the mean catchment slope angle.
[e] HI is the hypsometric index (mean elevation - minimum elevation/relief) of a catchment based on Strahler (1952).
[f] Precip. is the area-weighted mean of the average annual precipitation recorded from 1998–2009 for a catchment (from Bookhagen, 2013).
[g] Lithology (from de Verteuil et al., 2006), vegetation cover, and land modification (from Helmer et al., 2012) are the percentage of a catchment surface area composed of siliciclastic bedrock, covered by vegetation (0%, no cover, to 100%, complete cover), and land area modified by anthropogenic activity (0%, not urbanized or built area, to 100%, urbanized or built area), respectively.
[h] Stream gradient is the gradient of the stream channel measured upstream from the ^{10}Be sample location.
[i] Distance from tilt axis is the distance of the midpoint of a catchment from the tilt axis as defined in the text (see Fig. 2 for location). Negative and positive distance values indicate catchments to the west and east of the tilt axis respectively.

Table 2
Summary of cosmogenic ^{10}Be data.

Sample name[a]	Quartz	^{9}Be carrier	^{9}Be carrier	^{10}Be/^{9}Be	^{10}Be	Production rate	Applicable	Catchment
	Mass	Mass	Concentration	AMS ratio	Concentration	Catchment mean	Time range	Erosion rate
	(g)	(g)	(mg/g)	(10^{-15})[b]	(at/g_{qtz}) (10^4)[c]	(at/g_{qtz} yr^{-1})[d]	(ka)[e]	(mm/ka)[f]
T1	21.16	0.3546	1.354	32.71 ± 2.21	4.40 ± 0.16	2.71 ± 0.35	16.3	36.9 ± 4.9
T2	20.73	0.3550	1.354	15.50 ± 1.44	1.83 ± 0.04	2.80 ± 0.36	6.5	91.8 ± 11.9
T3	20.50	0.3451	1.354	24.11 ± 2.37	3.11 ± 0.18	2.78 ± 0.36	11.2	53.6 ± 7.5
T5	10.11	0.3486	1.354	14.66 ± 1.77	3.42 ± 0.18	3.23 ± 0.41	10.6	56.6 ± 7.9
T6	16.57	0.3500	1.354	32.43 ± 2.06	5.49 ± 0.17	3.20 ± 0.41	17.2	35.0 ± 4.6
T7	21.79	0.3511	1.354	69.75 ± 39.28	9.63 ± 5.55	3.40 ± 0.43	28.3	21.2 ± 12.5
T8	20.47	0.3571	1.354	47.89 ± 2.99	6.97 ± 0.28	3.40 ± 0.43	20.5	29.2 ± 3.9
T9	19.75	0.3557	1.354	24.93 ± 4.66	3.46 ± 0.56	3.37 ± 0.43	10.3	58.4 ± 12.1
T10	21.74	0.3635	1.354	46.48 ± 9.24	6.47 ± 1.21	3.11 ± 0.40	20.8	28.8 ± 6.6
T11	19.74	0.3596	1.354	55.64 ± 2.76	8.56 ± 0.26	3.12 ± 0.40	27.4	21.9 ± 2.9
T12	20.15	0.3458	1.354	24.99 ± 1.84	3.31 ± 0.10	2.86 ± 0.37	11.6	51.8 ± 6.8
Trin-BLK 1	0	0.3578	1.354	4.65 ± 1.51				
Trin-BLK 2	0	0.3554	1.354	2.72 ± 0.84				
T18	25.43	0.3465	1.414	77.73 ± 7.92	8.24 ± 0.70	2.78 ± 0.36	29.7	20.2 ± 3.1
T19	26.89	0.3485	1.414	139.77 ± 11.77	15.44 ± 1.14	2.83 ± 0.36	54.5	11.0 ± 1.6
T20	27.32	0.3490	1.414	92.96 ± 5.03	9.57 ± 0.31	2.69 ± 0.34	35.6	16.8 ± 2.2
T21	28.08	0.3446	1.414	85.83 ± 7.70	8.36 ± 0.60	2.83 ± 0.36	29.6	20.3 ± 3.0
T22	28.61	0.3647	1.414	47.26 ± 5.65	4.04 ± 0.38	2.85 ± 0.36	14.2	42.3 ± 6.7
T23	28.90	0.3559	1.414	43.06 ± 5.20	3.42 ± 0.32	2.97 ± 0.38	11.5	52.2 ± 8.2
T24	26.33	0.3436	1.414	29.51 ± 4.30	1.95 ± 0.22	2.98 ± 0.38	6.5	91.8 ± 15.7
T27	27.17	0.3540	1.414	46.21 ± 4.70	4.00 ± 0.27	2.67 ± 0.34	15.0	40.1 ± 5.8
T28	26.35	0.3435	1.414	31.50 ± 2.60	2.19 ± 0.01	2.87 ± 0.37	7.6	78.7 ± 10.1
T29	27.36	0.3666	1.414	54.65 ± 7.32	5.18 ± 0.61	2.85 ± 0.36	18.2	33.0 ± 5.7
T30	26.81	0.3669	1.414	33.42 ± 3.25	2.55 ± 0.10	2.85 ± 0.36	9.0	67.0 ± 8.9
T32	26.87	0.3585	1.414	61.76 ± 3.18	6.06 ± 0.09	2.96 ± 0.38	20.4	29.3 ± 3.8
T33	25.77	0.3698	1.414	72.77 ± 5.33	8.01 ± 0.38	2.67 ± 0.34	30.0	20.0 ± 2.7
T34	27.20	0.3500	1.414	70.32 ± 5.19	6.88 ± 0.33	2.75 ± 0.35	25.1	23.9 ± 3.3
Trin-BLK3	0	0.3606	1.414	13.67 ± 3.88				
Trin-BLK4	0	0.3488	1.414	13.74 ± 1.11				
T25	30.57	0.3534	1.023	34.4 ± 2.49	2.59 ± 0.14	2.89 ± 0.37	9.0	67.0 ± 9.3
T40	29.80	0.3473	1.023	91.2 ± 4.04	7.14 ± 0.26	3.01 ± 0.39	23.7	25.3 ± 3.4
T41	30.29	0.3543	1.023	56.8 ± 3.37	4.42 ± 0.21	3.16 ± 0.40	14.0	43.0 ± 5.9
T42	30.41	0.3535	1.023	62.1 ± 2.74	4.81 ± 0.16	2.99 ± 0.38	16.1	37.3 ± 4.9
T45	30.11	0.3560	1.023	128.7 ± 20.25	10.27 ± 1.58	3.08 ± 0.39	33.3	18.0 ± 3.6
T47	24.23	0.3508	1.023	45.1 ± 4.23	4.30 ± 0.34	2.63 ± 0.34	16.4	36.7 ± 5.5
T48	29.59	0.3526	1.023	68.8 ± 3.44	5.48 ± 0.22	2.81 ± 0.36	19.5	30.8 ± 4.1
T49	23.49	0.3558	1.023	46.0 ± 4.08	4.59 ± 0.35	2.85 ± 0.37	16.1	37.3 ± 5.5
Trin-BLK5	0	0.3507	1.023	1.92 ± 0.78				
Trin-BLK6	0	0.3538	1.023	1.28 ± 0.71				
Average:	24.9	0.3537		54.8 ± 5.9	5.6 ± 0.5	2.9 ± 0.4	19.3	40.2 ± 6.2
Maximum:	30.6	0.3698		139.8 ± 39.3	15.4 ± 5.6	3.4 ± 0.4	54.5	91.8 ± 15.7
Minimum:	10.1	0.3435		14.7 ± 1.4	1.8 ± 0.0	2.6 ± 0.3	6.5	11.0 ± 1.6

Lal (1991) and Stone (2000) time-independent scaling framework and production rate of 4.01 ^{10}Be atoms g_{quartz}^{-1} y^{-1} (Borchers et al., 2016), and corrected for topographic shielding.

[a] BLK is a sample blank, processed and analyzed with the sediment samples listed in rows above.

[b] AMS is the accelerator mass spectrometer Be ratios and 1σ analytical uncertainty measured at PRIME lab, Purdue University, normalized with standards from Nishiizumi et al. (2007).

[c] Concentration of ^{10}Be is corrected with the mean of the sample blanks processed with corresponding samples and 1σ analytical uncertainty.

[d] Production rates and 1σ uncertainty calculated using MATLab (2009) are catchment-averaged from each pixel (30 m DEM), based on the.

[e] Applicable time range follows Lal (1991).

[f] Erosion rates are calculated with a ^{10}Be half-life of 1.36 ± 0.07 m.y. (Nishiizumi et al., 2007), an attenuation length of 0.6 m, and a shielding-corrected catchment-averaged production rate. The 1σ uncertainty is propagated from AMS analytical and production rate uncertainties.

when the quartz is derived from a beryl-bearing granite or pegmatite (Portenga et al., 2015), the indigenous ^{9}Be must be taken into account. Because pegmatites and beryl-bearing granites are not present in our study area, it is highly unlikely that any significant native ^{9}Be is present in our quartz. In the unlikely case that native ^{9}Be is present in our quartz, then it would provide overestimates of our erosion rates, making our rates even slower than we have calculated. Moreover, our calculations can be used as apparent erosion rates for comparisons of variation across our study area.

Riebe and Granger (2013) have shown that chemical weathering across different climate zones can produce erroneous erosion rate results, particularly in regions of high rainfall and humidity. Chemical weathering can enrich regolith with, and increase the residence time of, relatively insoluble minerals such as quartz, which could result in spuriously slow erosion rates (Riebe and Granger, 2013). We use the annual average precipitation as a proxy for the extent of chemical weathering in the Northern Range after the methods of Riebe and Granger (2013). The corrected data show the largest increases in erosion rates for the wetter catchments (in the east) and average an ~30% change (Table S1). Because these adjusted erosion rate data integrate precipitation, they pronounce the spatial trend of erosion rates increasing eastward and make statistical correlations stronger. We therefore use the uncorrected erosion rates for all analyses.

3.5. Topographic, geomorphic, and geologic analyses

Topographic and geomorphic metrics were calculated in ArcMap 10.1 from a 1-arc-second (30 m) DEM obtained from a USGS grid (ASTGDEMV2). This raw data grid was void filled to correct for gaps and modeled artifacts, e.g., cloud coverage or no data. Catchments were

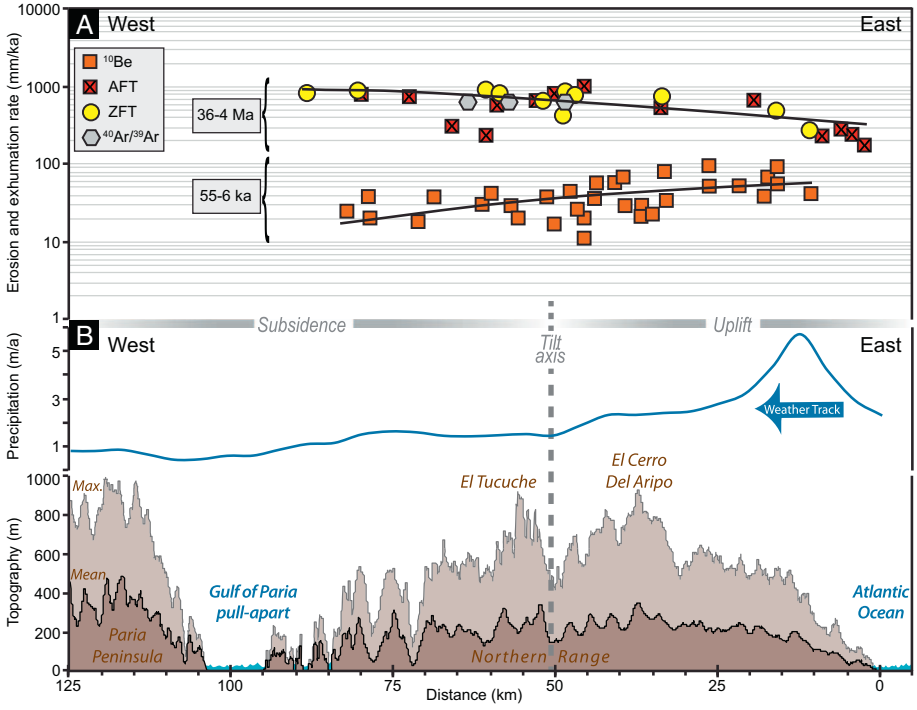

Fig. 4. East-west profiles across the Northern Range in Trinidad, Gulf of Paria, and eastern Paria Peninsula in Venezuela showing: (A) erosion and exhumation rates derived over multiple time scales including ^{10}Be data (this study) and thermochronology exhumation rates from apatite fission track (AFT; Weber et al., 2001b; Denison, 2008) and zircon fission track (ZFT; Algar et al., 1998; Weber et al., 2001b) ages and ^{40}Ar/^{39}Ar white mica metamorphic ages (Foland et al., 1992) with the best-fit linear regressions (black lines) to show the general data trends. Thermochronology data integrate over time periods of ~36–4 Ma and ^{10}Be data integrate over the last ~55–6 ka. (B) Average annual precipitation rates over the region (Bookhagen, 2013) and swath profiles of mean (dark brown) and maximum (light brown) topography showing differences across the tilt axis (grey dashed line) of relatively high elevation, low-relief topography to the east and high-relief, low elevation topography and drainage outlets to the west. Note the major reversal in the locus of erosion, with respect to the tilt axis and the order of magnitude difference of erosion rate over different time intervals. (For interpretation of the references to color in this figure legend, the reader is referred to the web version of this article.)

defined as the area upstream of the sample location (Figs. 2, 3), and metrics that were determined are in Table 1. Relative relief was calculated as the difference between the maximum and minimum elevations within a catchment. The distance from the tilt axis was measured as an orthogonal projection from the mid-point of each catchment to the tilt axis. Hypsometric indices were calculated as the difference between mean and minimum catchment elevations over the catchment relief (Strahler, 1952). A swath elevation profile was constructed over the entire N-S width of the Northern Range and eastern Paria Peninsula, straddling the long-axis of mountains (Fig. 4). The N-S width of the swath profile was defined by the coastline and by the range front at the inflection of the slope break and alluvial surface to the south (Fig. 3).

Longitudinal stream profiles were extracted from the 30-m-void filled DEM along the axis of stream channels from catchments where we collected cosmogenic ^{10}Be samples (n = 26) with basic profile extensions in ArcGIS (Figs. 3, 5, S2). We applied a best-fit polynomial curve (blue lines in Figs. 5, S2) to the raw elevation data (brown lines in Figs. 5, S2) of the stream profiles. This smoothing helps to reveal the long wavelength (~5–15 km) morphology of a stream channel that represents a major knick zone and in some channels the integration of perhaps several knickpoints. We refer to the inflection of the upper point of convexity in the smoothed stream profiles as knickpoints. Lithology from de Verteuil et al. (2006) was mapped on each stream profile to identify potential effects of rock type changes on the formation of knickpoints (Figs. 5, S2). Stream gradients were calculated from longitudinal profiles upstream of each ^{10}Be sample location (Table 1).

Lithological data are summarized as the percentage of surface area composed of quartz-rich bedrock in each catchment (Table 1). The metamorphic rock units (e.g., schist, phyllite, quartzite) of the Northern Range on the de Verteuil et al. (2006) map were grouped based on the abundance of quartz in varying lithologies and are termed here as siliciclastic (quartz-rich) vs. nonsiliciclastic (quartz-poor; e.g., carbonate schists, marbles, etc.). To test for the effect of quartz-poor lithology on erosion rates, we eliminated the catchment area covered by calcareous bedrock units. Erosion rates derived from this method changed by < 1% because of the small catchment areas that span very little change in latitude or elevation. Furthermore, quartz is sourced from the quartzite, quartz-schist, metasandstone, and metaconglomerate bedrock and is pervasive in all metasedimentary units in the form of late brittle quartz veins and veined zones that can be up to ~3 m wide.

3.6. Precipitation, vegetation, and modern land use analyses

Precipitation values were obtained from NASA's Tropical Rainfall Measuring Mission (TRMM) global data product 2B31, which was processed and spatially gridded by Bookhagen (2013; Figs. 2, 4). The mean-monthly TRMM precipitation records have a spatial resolution of ~4 km^2 and estimate mean-annual precipitation over an average of 12 years (1998–2009; Bookhagen, 2013). To account for variable precipitation rates within a catchment, we incorporate each pixel of the precipitation data that is bound within a catchment and derive an area-weighted mean (Table 1).

Vegetation cover and type and land use data were obtained from Helmer et al. (2012; Fig. 2). These data are from multiseason Landsat and multiseason fine-resolution imagery from periods over approximately a century (1927 to 2010) of measurements and are processed to a spatial resolution of 1-arc-second (30 m; Helmer et al., 2012). Nine land cover classifications relevant to this study were used to estimate the percentage of land developed by human activity and vegetation cover (Table 1). To assess land use we grouped these classifications into natural vegetation (montane forest, evergreen and semievergreen seasonal forest, dry evergreen, deciduous, and herbaceous and forested wetland) and modern altered land types (young secondary forest, agriculture, urban or built-up land, and nonvegetated). To assess vegetation cover we grouped all vegetation types to compare against urban or built-up and nonvegetated land (range from 0 to 100% vegetation coverage).

3.7. Correlation analyses of erosion rates and catchment metrics

Bivariate regression analyses were used to test the correlation of erosion with topographic, geologic, and environmental variables (Fig. 6; Table S2). Because erosion rates follow a nonlinear distribution in some cases (Portenga and Bierman, 2011), we use Spearman's product-moment correlation analysis. Multiple regression correlation analysis was also used to determine whether a combination of variables

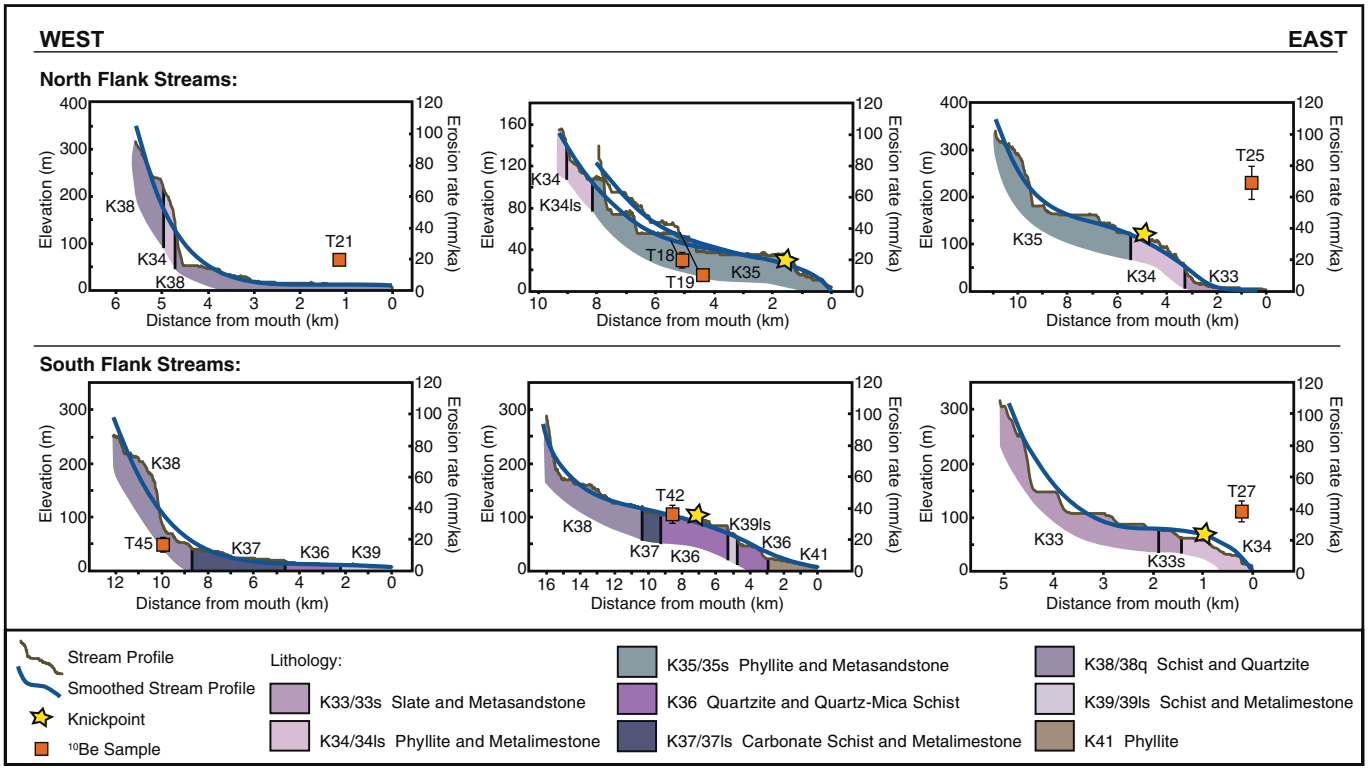

Fig. 5. Selected longitudinal stream profiles showing major knickpoints (stars), ^{10}Be catchment erosion rates with 1σ uncertainty (orange squares) and lithology (from de Verteuil et al., 2006), from streams draining the north flank (upper plots) and south flank (lower plots) of the Northern Range, arranged from west to east (left to right). Locations of all longitudinal stream profiles (n = 26) are shown in Fig. 3 and all measured profiles are given in supplementary material Fig. S2. (For interpretation of the references to color in this figure legend, the reader is referred to the web version of this article.)

could better explain variability in catchment erosion rate rather than a single variable. Data subsets were calculated based on the geographic location of a sample, which includes samples from stream mouths on the north versus south flank and from headwater locations (Table S2).

4. Results

4.1. Cosmogenic ^{10}Be catchment erosion rates results

Northern Range catchment-wide erosion rates based on ^{10}Be concentrations generally increase to the east by roughly eightfold and range from 11.0 ± 1.6 to 91.8 ± 15.7 mm/ka (Figs. 3, 4; Table 2). The average rate of catchment erosion is ~40 mm/ka, and the average 1σ uncertainty is ~6%. Replicate samples collected from the Aripo catchment, < 3 m apart, reproduced well within 1σ error (T7, 21.2 ± 12.5 and T8, 29.2 ± 3.9 mm/ka). The erosion rates derived here represent time spans from 54.5 to 6.5 ka (equations from Lal, 1991). Because erosion rates integrate over millennial timescales, throughout this paper we express erosion rates in units of mm/ka.

In six of the seven multisampled catchments, samples that were collected near the headwaters yield erosion rates that are higher than those downstream (Figs. 3, 5, S2). In two of these headwater locales, where stream sediment was collected just below (within ~5 m) major waterfalls (knickpoints), erosion rates are almost double those downstream — in the Arroyo Seco basin, T2 is 91.8 mm/ka and T3 is 53.6 mm/ka, and in the Tucker basin, T47 is 36.7 mm/ka and T33 is 20.0 mm/ka. The Madamas catchment is the only multisampled catchment that yielded a lower erosion rate for a sample collected upstream (T29 is 33.0 mm/ka) relative to a sample collected downstream (T28 is 78.7 mm/ka).

Lower erosion rates from samples collected at stream mouths could indicate that landslides or sediment mixing influences the distribution of sediment flux (Niemi et al., 2005; Yanites et al., 2009). However, following Niemi et al. (2005) and Yanites et al. (2009), the average catchment size sampled in the Northern Range was 22 km^2, and most of our samples were collected > 10 m downstream of inner-catchment tributaries to minimize the effects of large landslides on cosmogenic ^{10}Be concentrations and to ensure complete sediment mixing. Likewise, catchment area and erosion rate statistically do not correlate (r = 0.03, p = 0.8774; Fig. 6). Alternatively, higher erosion rates upstream may be an indication of aggressive upstream incision and transient headward propagation of knickpoints, given that these upstream samples were collected at the base or below several steep (near vertical) knickpoints (waterfalls). In addition, samples that came from the stream headwaters have, on average, steeper hillslope gradients (~20°) and stream gradients (~36 m/km) than those samples collected at a steam mouth, which have average hillslope gradients of ~18° and stream gradients ~25 m/km (Table 1). This is consistent with the statistically significant and positive correlation between erosion rate and stream gradient (r = 0.33, p = 0.0583; Fig. 6). The observation that most erosion rates from stream mouths are lower than those from headwaters may be an indication of a general downstream reduction of hillslope relief. It may also indicate that sediment is mixed downstream and incorporates sediment derived from lower gradient hillslopes and streams, which likely erode more slowly. Higher erosion rates from steep headwater locales have also been reported from other tropical catchments such as some of those in Brazil (e.g., Gonzalez et al., 2016a).

4.2. Spatial variability of catchment topography

Topographic relief is highest in the western and central Northern Range and is associated with summit elevations such as those of El Tucuche and Trinidad's highest peak El Cerro del Aripo (Fig. 4). Catchment-mean hillslope gradients average ~19° and generally decrease from west-to-east from 16–27° to 13–22°. Hypsometric indices

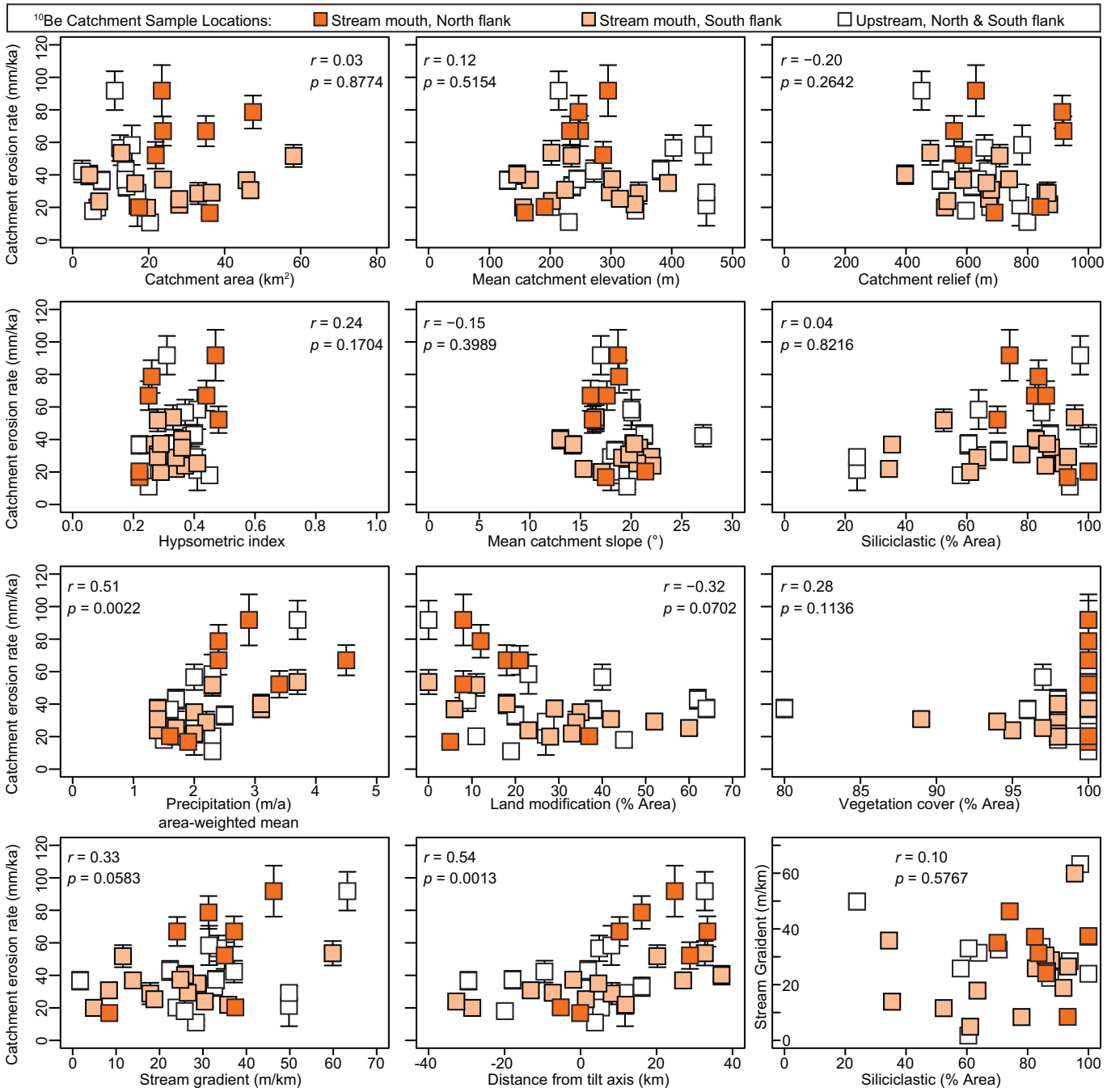

Fig. 6. Bivariate relationships between ^{10}Be catchment erosion rates (shown with 1σ uncertainty) and catchment metrics. Correlation coefficients and statistical significance shown here are for all catchment data and are given for subgroups in Table S2.

range from 0.22 to 0.48 and average 0.33 (Table 1). Catchments with the highest hypsometric values are located on the north and east flanks of the range where precipitation and postulated late-stage surface uplift rates are greatest (Fig. 4). The lowest hypsometric values are from catchments located in the proposed region of subsidence and lower relative precipitation on the south and west flank of the Northern Range.

Longitudinal stream profiles (n = 26) extracted from Northern Range catchments generally transition eastward from concave to convex (Figs. 5, S2). The smoothed stream profiles (blue lines in Figs. 5, S2) show a distinct difference in long wavelength channel geometry, with fully concave profiles located in the west and highly convex profiles located in the east. The raw elevation data show that knickpoints occur in concave and in convex streams (in the east and west) and that all streams contain multiple knickpoints (some > 10), yet these occur at varying elevations. Lithologic contacts and a particular rock type coincide with some knickpoints along stream profiles, but the same contact or lithology may not be associated with a knickpoint in a neighboring stream. For example, a prominent knickpoint (and convexity) occurs in the quartzite (K36) in the Diego Martin catchment (T45; Fig. 5), whereas in the Caura catchment (T42; Fig. 5) no knickpoint occurs in the quartzite and the stream profile is fully concave. Lithologic or structural contrasts do not appear to control the majority of knickpoints. Notably, in the region of proposed uplift in the east, knickpoints commonly occur at low elevations, from < 100 to 5 m amsl, and several are located ≤ 2 km from the stream mouth (e.g., catchments T18/19 and T27; Fig. 5). The occurrence of these low elevation knickpoints close to stream outlets likely represent the most

recent perturbation to the topography and may be an indication of young climatic, tectonic, or base-level changes.

Geomorphic metrics measured on the catchment-scale represent an integration of controls and processes (e.g., tectonics, erosion, climate, lithology, and preexisting structures) that can translate through the landscape over timescales on the order of 10^4–10^6 years (e.g., Strahler, 1952; Allen, 2008). We consider the metrics that we measured from the Northern Range to represent tectonic and climatic forcings that essentially occurred during the Quaternary. Certainly, complex variations in tectonic and climatic processes have occurred during the Quaternary in Trinidad, yet the catchment-scale geomorphic analyses we present likely characterizes the general tectonic trends and time-averaged glacial-interglacial climate cycles.

4.3. Correlations of cosmogenic ^{10}Be catchment erosion rates and catchment metrics

Bivariate regression analyses yield poor to moderate correlations between all of the catchment erosion rates and measured catchment metrics (Fig. 6; Table S2). Of the geomorphic metrics measured the only statistically significant variables ($p < 0.05$) are distance from the tilt axis ($r = 0.54$, $p = 0.0013$) and stream gradient ($r = 0.33$, $p = 0.0583$). Of the environmental metrics measured, precipitation is the only statistically significant variable ($r = 0.51$, $p = 0.0022$). The strength of some correlations increase when data subsets are evaluated based on the geographic location of the sample, but the limited sample size may influence these increases (Table S2). Feedbacks between some of the variables (e.g., precipitation and vegetation cover) that covary along-strike of the Northern Range make it challenging to isolate variables. This east-west covariance among several of the variables may also explain the moderate to strong multiple regression correlation coefficients. However, these multiple regression coefficients are statistically insignificant (all data, $R^2 = 0.48$, $p = 0.1237$; all data from catchment mouths, $R^2 = 0.69$, $p = 0.2459$; Table S2).

5. Discussion

The primary finding of this study is the low millennial-scale rates of erosion (~11–92 mm/ka). A global compilation of cosmogenic catchment-mean erosion rates yielded a global mean of ~200 mm/ka, over twice the maximum value that we measured here (Portenga and Bierman, 2011). Our new millennial-scale erosion rate data, combined with published thermochronology ages from the Northern Range, clearly show a marked difference in the style and tempo of erosion, and likely also surface uplift (Fig. 4). These data highlight distinct syn- and post-collisional phases of evolution of the Northern Range. A significant deceleration of erosion is consistent with the cessation of the Caribbean-South American plate collision, but it is striking that despite possibly rapid rates of Quaternary surface uplift and high rainfall, our millennial erosion rates are so low.

5.1. Evidence of post-collisional tectonic tilting and transient erosion

The combined thermochronology and cosmogenic nuclide data document a major inversion and deceleration of erosion of the Northern Range, which is consistent with the relative change from oblique-convergence to transform Caribbean-South American plate motion. Longer-term exhumation rates from apatite and zircon fission-track thermochronology (Algar et al., 1998; Weber et al., 2001b; Denison, 2008) and ^{40}Ar/^{39}Ar ages (Foland et al., 1992) shows that exhumation rates from ~37 to 4 Ma are over an order of magnitude higher than our new ^{10}Be-derived erosion rates, which integrate over millennia from ~55 to 6 ka (Fig. 4). Plate reconstructions and contractile structures in central and southern Trinidad indicate that this region was dominated by oblique Caribbean-South American plate convergence until ≤10 Ma (Speed, 1985; Pindell et al., 1998; Giorgis et al., 2016). The resulting NW-SE contraction is also generally thought to have caused deformation and driven asymmetric exhumation of the Northern Range (Frey et al., 1988; Algar et al., 1998; Weber et al., 2001b; Cruz et al., 2007; Denison, 2008). This asymmetry is reflected in younger thermochronology ages in the western Northern Range and eastern Paria Peninsula, and rocks that decrease in metamorphic grade and contain less ductile structures and fabrics eastward (Frey et al., 1988; Foland et al., 1992; Algar and Pindell, 1993; Algar et al., 1998; Weber et al., 2001b).

In the late Miocene, the Caribbean-South American plate boundary stepped southward and changed to its current phase of transform plate motion, which is now focused along the Central Range Fault some 30 km south of the Northern Range (Algar and Pindell, 1993; Pindell et al., 1998; Babb and Mann, 1999; Weber et al., 2001a). A right-step of the El Pilar-Central Range Fault in the plate boundary zone developed a transtensional pull-apart basin in the Gulf of Paria in eastern Venezuela and western Trinidad (Figs. 1, 3; Babb and Mann, 1999; Flinch et al., 1999). Based on numerous lines of qualitative geomorphic evidence, Weber (2005) proposed range-wide tilting of the Northern Range during the Quaternary driven by subsidence into the Gulf of Paria pull-apart basin. The order of magnitude deceleration in erosion over the period of the major change in relative plate motion is consistent with less tectonic flux, i.e., less convergent material input, along the transform boundary that developed to the south of the Northern Range. We consider additional factors that could dampen the magnitude of erosion rates in the next sections.

The spatial pattern of our ^{10}Be-derived erosion rates and new geomorphic analyses suggest a vertical tectonic inversion of the Northern Range that was post-collisional and is consistent with Quaternary range-wide tiling (Fig. 7). In principal, tectonic tilting should cause enhanced erosion in the eastern catchments relative to those in the west (e.g., Cyr et al., 2010; Gudmundsdottir et al., 2013). Increases in erosion rates driven by rock uplift can occur through a variety of processes including enhanced stream incision and erosion in response to base-level changes and landsliding as hillslopes adjust to steepening (e.g., Wobus et al., 2010). Tectonic subsidence is not resolvable in the ^{10}Be data, but changes in sedimentation accumulation in the basins surrounding the Northern Range could potentially be used to document and study subsidence (e.g., Bonnet and Crave, 2003).

The eastward increase of our millennial-scale erosion rate data spatially correlates well with Weber's (2005) proposed late-stage west-to-east tectonic transition from subsidence to uplift (Figs. 3, 4, 7). However, the erosion rate gradient also spatially correlates with the strong modern west-to-east precipitation gradient. Our bivariate correlation analysis indicates that our proxy for recent tectonics (i.e., distance from the tilt axis) is a more powerful regressor ($r = 0.54$) for explaining erosion rate variations than precipitation ($r = 0.51$), but differences between these two coefficients are small and may be insignificant relative to sample size and uncertainty (Fig. 6; Table S2). In addition, these bivariate statistical correlations are moderate and our proxy for recent tectonics and precipitation covary eastward. Distinguishing a dominant control between either late-stage tectonic and climatic forcing factors on erosion is therefore challenging from our limited samples and statistical comparison.

Quaternary tectonic tilting, however, appears to be driving the broad, mountain-scale spatial distribution of topography (Figs. 4, 7). This inference is qualitatively supported by the presence of elevated Quaternary marine terraces and alluvial fans that are present and/or exposed only in the east. In addition, mountain front and coastal sinuosity straighten eastward and drainage outlet elevations increase eastward (Weber, 2005; Ritter and Weber, 2007). The absence of marine terraces in the west does not exclude the possibility that they may have formed there but have not been persevered. However, submerged catchment valleys, particularly those in the Dragon's Mouth Passage, are strong evidence of subsidence in the west. Likewise, higher precipitation in the east could be responsible for the Quaternary alluvial fans bounding the eastern mountain front, yet the correlative

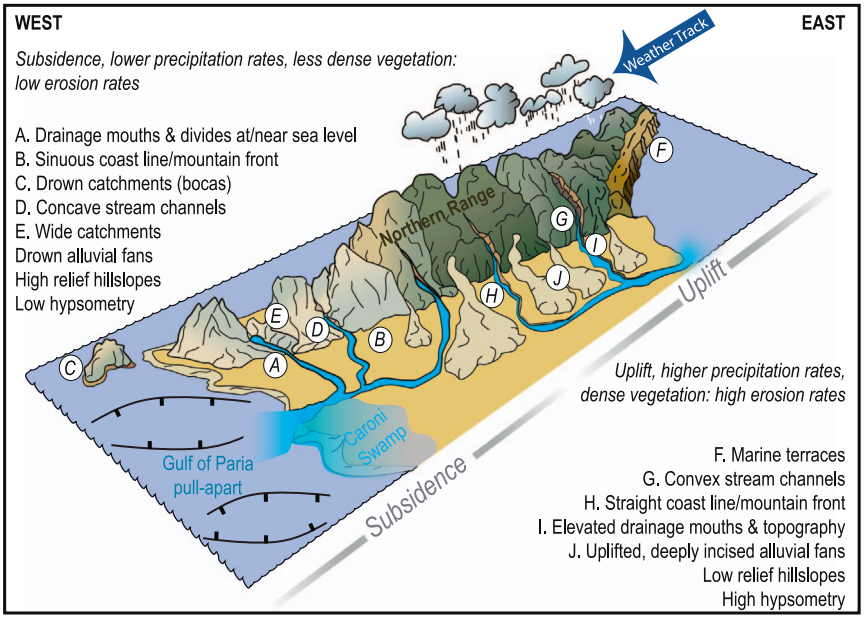

Fig. 7. Schematic diagram showing landforms of the Northern Range and likely controlling Quaternary processes (modified from Weber, 2005; Ritter and Weber, 2007). Note that late-stage tectonic tilting transitions east-to-west resulting in emergent (east) and submergent (west) coastlines and landscapes that are also influenced by westward decreases in precipitation, vegetation density, and erosion rates.

alluvial units are present in the west but they have been sunken to depths over ~100 m and are covered by the Caroni Swamp (Ritter and Weber, 2007). Mountain front sinuosity could be influenced by lithologic changes, but we conclude that there are no significant differences in erodibility given that the mountain flanks consist of rocks of similar metamorphic character and that we observe a statistically very weak and insignificant ($r = 0.04$, $p = 0.8216$) correlation between erosion rate and lithology (Fig. 6).

Northern Range topography shows significant eastward increases in mean catchment elevation and hypsometry but also an eastward decrease in mean hillslope relief (Figs. 4, 7). These hillslope changes indicate that as precipitation increases, hillslope gradients and relief are generally reduced, which is consistent with the view that a wetter climate leads to a decrease in relief (Bonnet and Crave, 2003; Wobus et al., 2010). Our hypsometric analysis also shows that the low-relief topography in the east is elevated despite the high precipitation and erosion rates there (Fig. 4). These relationships suggest that while the precipitation may be controlling hillslope angles, east-side-up tilting is controlling the bulk distribution of topography. These two processes likely act together to generate the elevated, yet subdued, relief located under the high rainfall and uplifted region of the eastern Northern Range and also the relatively higher relief but low elevation topography in the west (Fig. 7).

The systematic change of longitudinal stream profile geometries is another indication that late-stage east-side-up tilting of the Northern Range is likely the process controlling the bulk distribution of topography. Stream profiles transition eastward from concave to convex (Figs. 5, S2). Although some knickpoints observed in the field (e.g., meter-scale waterfalls) occur at lithologic transitions, lithology does not appear to control the overall shape or large convexities of stream profiles. This inference is supported by the lack of a correlation between rock type and channel gradient (Fig. 6). Precipitation is also probably not generating these broad west-to-east stream profile transitions, as high precipitation in the east would likely promote aggressive stream incision (e.g., Wobus et al., 2010), reducing stream gradients and knickpoints, which is contrary to the convex and high gradient streams observed there. A change of climatic conditions or a relative drop in sea level could generate knickpoints and convex stream profiles, yet these regional-scale processes should drive stream profile geometries to change equally in one direction (all convex or all concave) across the mountain range. In addition, our erosion rates average over time periods when sea level was generally rising. Low elevation knickpoints (< 100–5 m amsl) located near stream outlets (within ~2 km) are common in the east but lacking in the west; this observation is also consistent with east-side-up tilting (e.g., catchments T18/19 and T27; Fig. 5). The majority of knickpoints and major convex inflections of stream profiles did not likely form because of spatial contrasts in erodibility, climate, or sea-level fall. We suggest that the stream geometries and knickpoints are strong evidence for post-collisional tectonic tilting of the Northern Range.

The presence of convex longitudinal stream profiles, moderately high hypsometric values, and low-elevation knickpoints in combination with low erosion rates indicate two important points (i) surface uplift of the eastern Northern Range is relatively young, and (ii) Northern Range erosion is in a transient state. The ages of marine terraces along the north and northeast coasts, perched at elevations of ~13 and ~21 m amsl, that are capped by Quaternary sediments (Kugler, 1959) are ~40 and 74 ka, respectively (Morell, 2009). Corrected for paleo-sea level, surface uplift rates in those areas may range from ~1000 to 3000 mm/ka. If uplift rates have been roughly monotonic, the highest terrace flight observed in the east (~45 m amsl) would indicate that uplift has occurred at least within the past ~100 ka. These relationships suggest that catchment erosion rates (~11–92 mm/ka) might significantly lag behind surface uplift rates by possibly over an order of magnitude during the Quaternary. The timing of late-stage uplift, initiating since at least ~100 ka and the transient morphology of hillslopes and erosion rates have significant implications for understanding the controls on landscape evolution and the cause(s) driving late-stage tilting of the Northern Range.

5.2. Transient erosion and post-collisional landscape adjustment

The westward decrease of the ^{10}Be-derived erosion rates indicates that erosion has responded to and reflects the spatial pattern of late-stage tectonic tilting and the precipitation gradient across the Northern Range (Figs. 4, 7). However, the order of magnitude difference between the catchment erosion and surface uplift rates and the presence of transient longitudinal stream profiles and knickpoints indicate that erosion is in a transient state in the Northern Range. These low rates of erosion (~11–92 mm/ka) are somewhat surprising given that the Northern Range experiences intense tropical precipitation (> 5 m/a) and weathering and has been subjected to a rejuvenated phase of rapid tectonic tilting (possibly ≥ 1000 mm/ka). Because the strongest evidence of transient erosion is in the eastern Northern Range, where

erosion rates integrate over the past ~17–6 ka, we next consider influences that may buffer erosion during this specific time interval, which is characterized by the Pleistocene–Holocene paleoclimate transition to a relatively warmer and wetter climate and associated rising sea level (Peterson et al., 2000; Haug et al., 2001; Peltier and Fairbanks, 2006).

The fluvial response to rising sea level is the aggradation of sediment in stream channels and a commensurate decrease in hillslope erosion (Allen, 2008; Wobus et al., 2010). Ramcharan (2004) documented evidence from Trinidad's wetlands that Holocene sea-level rise caused the islands' rivers to aggrade and that many of the coastal wetlands were created and modified during this period of time. Eustatic sea-level rise could contribute to the low erosion rates we observe in Northern Range catchments, but it cannot explain the coevolution of convex longitudinal stream profiles and knickpoints — these features are typically attributed to a relative drop in sea level (e.g., Wobus et al., 2010). In addition, fluvial networks may have been somewhat insulated from the effects of rising sea level, given that the shallow and gentle slope of the South American continental shelf that surrounds the Northern Range reaches depths of only ~30 m in the Gulf of Paria and that the 100-m isobath of the shelf extends ~50 km north of the range (Fig. 1).

Paleoclimate records from the Cariaco Basin in Venezuela indicate an increase in precipitation during interstadials that followed the Pleistocene-Holocene climatic transition (Peterson et al., 2000; Haug et al., 2001). An intensification of rainfall should enhance hillslope erosion and would likely cause a reduction of hillslope relief and stream channel gradients (Bonnet and Crave, 2003; Wobus et al., 2010). However, the low rates of catchment erosion and the occurrence of convex stream profiles, knickpoints, and moderately high hypsometry of the eastern Northern Range are all in opposition to the expected effects of enhanced precipitation.

High precipitation and humidity can, however, increase the efficiency of chemical weathering and also lead to the formation of saprolite. These processes can protect from the physical removal of bedrock in several ways, including dilution of sediments and by forming porous regolith, which counteracts rainfall by reducing overland flow (e.g., Pelletier et al., 2013). High weathering fluxes and saprolite development over millennial scales are documented in Puerto Rico and Brazil, which are located in a similar climatic setting as the Northern Range; studies at both of these locations also yielded low rates of erosion (White et al., 1998; Riebe et al., 2003; Pupim et al., 2015). However, based on our data, influences such as these remain unclear in the Northern Range. Although it appears that lithology does not affect the spatial pattern of erosion (Fig. 6), significant groundwater recharge is evident by the presence of productive aquifers in the Northern Range, which are critical sources of drinking water on the island (WRA, 2001). We have approximated the extent of chemical weathering by using modern precipitation as a proxy (methods after Riebe and Granger, 2013), but the maximum change of the ^{10}Be-derived erosion rates from the wettest catchments are still more than six times lower than Quaternary surface uplift rates (Table S1). At present, the effects of chemical weathering and saprolite development do not appear be the primary cause of, but they do likely contribute to, the reduction of hillslope erosion in the Northern Range.

Increased precipitation driven by a transition to a warmer and wetter climate also could have caused changes in vegetation type and cover, which could significantly moderate the rate of hillslope erosion (e.g., Istanbulluoglu and Bras, 2005; Vanacker et al., 2007; Pelletier et al., 2013). Acosta et al. (2015) showed that erosion rates in East Africa are about twice as high in catchments that are sparsely vegetated when compared to those in more densely vegetated catchments. Likewise, Olen et al. (2016) showed a strong dependence between hillslope erosion rates and vegetation density in Himalayan catchments. Quaternary vegetation changes in the Northern Range are unknown, yet Hughen et al. (2004) documented that the vegetation in the Cariaco region in northern Venezuela shifted rapidly from arid grassland to wet forest during global deglaciations. A similar increase in vegetation cover and transition to denser vegetation assemblages might reasonably have occurred in the Northern Range during the Pleistocene-Holocene climatic transition.

Low rates of erosion measured over millennia have been documented in many other tropical landscapes (e.g., von Blanckenburg et al., 2004; Vanacker et al., 2007; Pupim et al., 2015). Gonzalez et al. (2016a) recently summarized and highlighted low rates of erosion in tropical settings derived from ^{10}Be data, including other Caribbean islands and neighboring South America regions (e.g., the Amazon River Basin, Panama, Bolivia, Puerto Rico, and Brazil). The average erosion rate we determined for Northern Range catchments (~40 mm/ka) is lower than those from the outlet of the central Amazon (~240 mm/ka; Wittmann et al., 2011), Panama (~158–201 mm/ka; Nichols et al., 2005; Portenga and Bierman, 2011; Gonzalez et al., 2016b), and Bolivia (360 mm/ka; Wittmann et al., 2009; Insel et al., 2010). In contrast, the average erosion rate for Northern Range catchments is higher than the average of all Brazilian watersheds (~10–14 mm/ka; Gonzalez et al., 2016a, 2016b, and references therein). The average erosion rate for Northern Range catchments is comparable to those measured in Puerto Rico catchments (~61 mm/ka; Brown et al., 1995, 1998; Riebe et al., 2003). Notably, all of these study sites are located in a range of tectonic settings, from passive margins to tectonically active, and perhaps highlight the suppressing effect vegetation has on hillslope erosion.

Given the apparently strong influence of vegetation on erosion, it is perhaps unexpected that we find our highest erosion rates in the densely vegetated hillslopes in the eastern Northern Range. However, based on feedbacks between precipitation and the growth of protective vegetation (e.g., Istanbulluoglu and Bras, 2005; Pelletier et al., 2013), we consider this to be another indication that tectonic tilting, rather than precipitation, is governing the spatial pattern of erosion and driving higher erosion rates in the east. In addition, unlike the results from the study of Acosta et al. (2015), for example, who nicely showed significant erosion rate variability in catchments covered by tropical forest versus those on patchy and barren hillslopes, the vegetation transitions westward in the Northern Range from tropical forest to deciduous forest — shifts that are not that extreme. On the basis of remote sensing data, hillslopes across the Northern Range are almost completely covered by some type of vegetation (Fig. 2). This implies that the impact of vegetation on erosion rates may be close to constant across the entire range. We suggest that vegetation cover may be a primary factor in buffering Northern Range hillslopes from tectonic or climatic perturbations, which is consistent with the uniformly low rates of hillslope erosion that we present here.

The transient state of erosion and geomorphology observed in the Northern Range is best explained by recent tilting in combination with dense vegetation, thick regolith, and porous lithology, which all appear to buffer erosional responses to tectonic or climatic perturbations (Fig. 7). The presence of elevated topography, convex longitudinal stream profiles, and knickpoints imply that topography was uplifting in the eastern Northern Range during the Quaternary, perhaps in concert with heavy and increasing rainfall. A transition to a wetter and warmer climate may have initially enhanced hillslope erosion, but also could have initiated the development or enhancement of dense vegetative cover and thick saprolite. Despite high magnitude precipitation, the uplifting hillslopes were (and are) well armored, preserving the oversteepened (convex) stream profiles, knickpoints, and elevated topography in the eastern Northern Range and the high relief hillslopes in the west. The presence of these landforms indicates that although erosion of Northern Range hillslopes may be buffered, the landscape has the capacity to record and preserve east-to-west spatial differences in post-orogenic tectonism. The combined cosmogenic erosion rate data, thermochoronology data, and geomorphic analysis indicate that a differential vertical tectonic signal that occurred ~100 ka and possibly over a few million years ago, has been preserved in the landscape. In

contrast, it seems that several factors, perhaps most importantly dense vegetation, buffers an erosional response such that it may take more than at least ~100 ka for erosion and hillslopes to fully adjust to the magnitude of surface uplift in this tropical mountain range.

5.3. Causes of post-collisional tectonic tilting

Distinctive faults that could accommodate Quaternary range-wide tilting of the Northern Range seem to be lacking. Most of the faults that bound and dissect the Northern Range show no geologic evidence of Quaternary activity (Algar and Pindell, 1993; Weber et al., 2001b, 2011). In addition, seismicity under the Northern Range is diffuse, and geodetic studies indicate that modern plate motion is concentrated ~30 km to the south of the Northern Range on the Central Range Fault (Fig. 3; Weber et al., 2001a, 2011; Churches et al., 2014). The tectonics of this region are also influenced by the transition from westward subduction of the oceanic South American plate to strike-slip motion between the continental South American and oceanic Caribbean plates (Fig. 1; Molnar and Sykes, 1969; Russo and Speed, 1992; Levander et al., 2014).

Quaternary uplift of the eastern Northern Range could potentially be driven by feedbacks between focused erosion and isostasy, given that higher rainfall occurs on the windward (eastern) side of the range. In addition, our work documents that greater erosional unloading should occur in the east. If we consider the case that the Northern Range is geodynamically supported via Airy conditions, then isostatic uplift should be proportional to ~80% of the volume of sediment removed (Turcotte and Schubert, 2014). Given that the catchment erosion rates and the marine terrace ages generally integrate over the same time scales, we conjecture whether the ~21-m-high marine terrace surfaces could have formed exclusively by erosional unloading since their formation ~74 ka. However, at the highest rates of catchment erosion we calculate over Quaternary timescales (~92 mm/ka), erosional unloading can account for only ~5 m of isostatic uplift. These relationships likely preclude erosional unloading as having a significant impact on the Quaternary uplift of the eastern Northern Range.

Ritter and Weber (2007) imagined the Northern Range to be a quasi-rigid block, which in response to subsidence in the Gulf of Paria elastically rebounded at its periphery causing flexural uplift of the eastern Northern Range. The major deceleration of erosion and the vertical tectonic inversion documented in the western Northern Range that occurred since the mid-Pliocene is consistent with the development of transtensional basins to the south and west of the range as a result of a southward step in the transform plate boundary (Babb and Mann, 1999; Flinch et al., 1999). Steeply dipping normal faults control half-grabens that are filled with late Miocene to Pliocene sediments and mark extension in the Gulf of Paria (Babb and Mann, 1999; Flinch et al., 1999). These structures are mapped from the Gulf of Paria to eastern Venezuela, south of the El Pilar Fault, and into the central Northern Basin in Trinidad (Fig. 1; Flinch et al., 1999). The western Northern Range, where we observe geomorphic evidence for subsidence, is consistent with the known regional extent of pull-apart-related extension.

Extension in the Gulf of Paria and east-side-up tilting of the Northern Range might also be influenced by deep geodynamic processes (Alvarez, 2014). Offshore, north of the Paria Peninsula and El Pilar plate boundary fault in northeastern Venezuela, the *Paria Cluster* of seismicity is interpreted to mark the location of deep lithospheric detachment (star in Fig. 1; Molnar and Sykes, 1969; Russo and Speed, 1992; Levander et al., 2014). Detachment of the oceanic South American lithosphere is proposed to accommodate subduction along the positively buoyant continental South American lithosphere by way of slab break-off (e.g., Russo et al., 1993; VanDecar et al., 2003; Marshall and Russo, 2005) or deep lithospheric tearing (e.g., Molnar and Sykes, 1969; Govers and Wortel, 2005; Clark et al., 2008a, 2008b). Broadband seismic data (Clark et al., 2008a; Levander et al., 2014) and surface wave tomography (Miller et al., 2009) show that the continental lithosphere to the south and west of the Paria Cluster and El Pilar Fault is significantly thinner and is bent northward toward the plate boundary by ~10–12 km relative to its position in the interior of the South American craton. Geodynamic models invoke partial removal of continental lithosphere along the plate boundary (Bezada et al., 2010; Levander et al., 2014) and show that asthenosphere flows around the edge of the subducting South American slab (Miller and Becker, 2012). Differences between extremely negative Bouguer and free air gravity anomalies indicate that the surface topography of the Paria Peninsula coastal range (the Northern Range's equivalent) in Venezuela is anomalously low, possibly ~3 km lower than expectations for Airy compensation (Russo and Speed, 1992). Asthenospheric flow, thinned lithosphere, viscous slab coupling, isostasy, and flexural bulging are hypothesized to be significant drivers of orogenesis and subsidence along the plate margin (Clark et al., 2008a, 2008b, 2008c; Miller et al., 2009; Alvarez, 2014).

Govers and Wortel (2005) modeled the geodynamic response to a deep lithospheric detachment along a near-vertical tear that extends through the lithosphere and propagates laterally in a direction opposite to that of subduction, calling this a subduction-transform edge propagator (STEP) fault. Their model showed that stresses focused at the edge of the STEP fault can cause significant downward flexure of the lithosphere and topographic subsidence along a transform plate boundary. Subsiding topography — which extends from the western Northern Range, across the Gulf of Paria, and to the eastern Paria Peninsula of Venezuela — is located over the region of predicted downward lithospheric deflection (Figs. 1, 4). Symmetric subsidence relative to the center of the Gulf of Paria is indicated by increases of catchment asymmetry, the elevation of drainage divides and drainage outlets, and the elongation of catchments on the peripheries of the region (Fig. 4; Ritter and Weber, 2007). In front of a STEP edge, lateral lithospheric resistance to tear propagation can cause upward flexural bulging of the lithosphere and surface uplift prior to tearing, over horizontal distances of a couple hundreds of kilometers (Govers and Wortel, 2005; Clark et al., 2008c). The uplifted eastern Northern Range, located ~100 to 160 km east, occurs well within these expectations. The observed vertical changes in topography across the Northern Range are also within the range of amplitudes (hundreds of meters to several kilometers) that may be associated with STEP fault deformation (Govers and Wortel, 2005).

Lithospheric detachment processes are proposed to be associated with subduction along this plate boundary for at least the past ~10 m.y. (Clark et al., 2008c; Miller and Becker, 2012). Given that crustal deformation currently occurs within an ~100-km radius of the proposed tear edge (Clark et al., 2008c) and assuming modern relative plate motion rates, a tear edge should have arrived near the eastern Paria Peninsula roughly in the late Pliocene. This timing generally coincides with the late Miocene to early Pliocene development of transtension (Babb and Mann, 1999; Flinch et al., 1999) and inception of the Gulf of Paria pull-apart basin (Weber, 2005). The southward step of the plate boundary and transtension in the Gulf of Paria could have been facilitated in part by the arrival of a STEP fault (Alvarez, 2014), though the development of a right-step is consistent with other influences, including a weakened Jurassic rifted margin, irregularities along the continent, and variations in lithospheric thickness (Molnar and Sykes, 1969; Babb and Mann, 1999; VanDecar et al., 2003). Regardless of the mechanism(s) for the southward step in the plate boundary, the initiation of extension in the Gulf of Paria and the arrival of a STEP fault are consistent with a Pliocene tectonic inversion of the Northern Range shown by our combined thermochronology and cosmogenic nuclide-based erosion rate data (Fig. 4).

Our data do not, however, uniquely distinguish the tectonic causes for the post-Pliocene inversion of the Northern Range. Extensional collapse of the shallow crust in the Gulf of Paria region, from the eastern Paria Peninsula to the western Northern Range, may be driven

in part by transtension related to the right-step from the El Pilar to Central Range plate boundary transform faults. Subsidence into the pull-apart basin could in principle cause flexural uplift of the eastern Northern Range. At depth, geodynamic processes related to deep lithospheric detachment could result in asthenospheric flow and dynamic topography. Either or both of these processes could drive extension and subsidence in the western Northern Range and cause upward lithospheric flexure on the peripheries, such as the young surface uplift we observed in the eastern Northern Range.

6. Conclusions

Cosmogenic ^{10}Be analysis from sediments in Northern Range catchments reveals low rates of millennial-scale erosion (averaging ~40 mm/ka) that increase eastward across the mountain range by roughly eightfold (from 11 to 92 mm/ka). The eastward increase of millennial-scale erosion rates coincide spatially with east-to-west changes of mountain morphology and are consistent with Quaternary east-side-up tilting of the Northern Range. We find that the highest millennial-scale erosion rates lag behind Quaternary surface uplift rates and occur in catchments with highly convex longitudinal stream profiles and relatively higher hypsometric values. These relationships indicate transient Quaternary erosion of the Northern Range. We suggest that hillslope adjustment and erosion of the Northern Range is buffered from climatic and tectonic forcings by dense tropical vegetation cover, thick saprolite, and porous regolith.

Compared with published long-term exhumation rates derived from thermochronometers, there has been over an order of magnitude deceleration of and shift in the locus of erosion in the Northern Range since the Pliocene. We suggest that these data mark an inversion of tectonism and highlight two major phases of Northern Range deformation and landscape evolution. The most intense period of dynamic mountain building included the unroofing of deeply buried metamorphic rocks and active crustal shortening and thickening, which occurred during the Mio-Pliocene. This period was characterized by NW-SE contraction and oblique collision between the Caribbean and South American plates. Thereafter, a significant change in the distribution of tectonism and tempo of erosion is consistent with the late Miocene change to transform plate motion and a shift of the plate boundary southward of the Northern Range. We interpret that post-collisional tectonism inverted the Northern Range with westward subsidence and eastward uplift. This second phase of development may be associated with the initiation of extension in the Gulf of Paria region and deep lithospheric detachment and mantle flow beneath the Paria Peninsula and associated dynamic topography.

Acknowledgements

Sincere thanks goes to three anonymous reviewers and editor Richard Marston for their very positive and constructive comments. We also sincerely thank Philip Farfan for help with sample collection critical to this study, for geologic discussions, and logistical support in the field. We thank those who aided with sample collection including Sekayi Liburd, Adrian Thomas, Carleen Webster, Harrison Gray, Mike Rutherford, and Paul Shaw. Rebecca Potter and Kathryn Hedrick are thanked for assistance with sample preparation at the University of Cincinnati Cosmogenic Lab. Support with graphics from Timothy Phillips at the University of Cincinnati is greatly appreciated. We thank the staff at PRIME lab, Purdue University, for performing AMS measurements. MWC acknowledges support from NSF (EAR0844151). Funding for this project was provided by the University Research Council of the University of Cincinnati as a Graduate Student Research Fellowship granted to LAO and JCA.

Appendix A. Supplementary data

Supplementary data to this article can be found online at http://dx.doi.org/10.1016/j.geomorph.2017.07.013.

References

Acosta, V.T., Schildgen, T.F., Clarke, B.A., Scherler, D., Bookhagen, B., Wittmann, H., von Blanckenburg, F., Strecker, M.R., 2015. Effect of vegetation cover on millennial scale landscape denudation rates in East Africa. Lithosphere 7 (4), 408–420.
Algar, S., Pindell, J., 1993. Structure and deformation history of the Northern Range of Trinidad and adjacent areas. Tectonics 12 (4), 814–829.
Algar, S., Heady, E.C., Pindell, J.L., 1998. Fission-track dating in Trinidad: implications for provenance, depositional timing and tectonic uplift. Paleogeographic Evol. Non-Glacial Eustasy North. S. Am. 58 (1), 111–128.
Allen, P.A., 2008. Time scales of tectonic landscapes and their sediment routing systems. Geol. Soc. Lond., Spec. Publ. 296 (1), 7–28.
Alvarez, T.G., 2014. The Southeastern Caribbean Subduction to Strike-slip Transition Zone: A Study of the Effects on Lithospheric Structures and Overlying Clastic Basin Evolution and Fill. Ph. D. Dissertation The University of Texas at Austin (257 p.).
Babb, S., Mann, P., 1999. Structural and sedimentary development of a Neogene transpressional plate boundary between the Caribbean and South America plates in Trinidad and the Gulf of Paria. In: Mann, P. (Ed.), Sedimentary Basins of the World. 4. Elsevier, pp. 495–557.
Balco, G., Stone, J.O., Lifton, N.A., Dunai, T.J., 2008. A complete and easily accessible means of calculating surface exposure ages or erosion rates from ^{10}Be and ^{26}Al measurements. Quat. Geochronol. 3 (3), 174–195.
Beard, J.S., 1946. The Natural Vegetation of Trinidad. Oxford University Press, Oxford.
Bezada, M.J., Levander, A., Schmandt, B., 2010. Subduction in the southern Caribbean: images from finite-frequency P wave tomography. J. Geophys. Res. Solid Earth 115 (12).
Bierman, P., Steig, E.J., 1996. Estimating rates of denudation using cosmogenic isotope abundances in sediment. Earth Surf. Process. Landf. 21 (2), 125–139.
von Blanckenburg, F., Hewawasam, T., Kubik, P.W., 2004. Cosmogenic nuclide evidence for low weathering and denudation in the wet, tropical highlands of Sri Lanka. J. Geophys. Res. Earth Surface 109, F03008.
Bonnet, S., Crave, A., 2003. Landscape response to climate change: insights from experimental modeling and implications for tectonic versus climatic uplift of topography. Geology 31 (2), 123–126.
Bookhagen, B., 2013. High Resolution Spatiotemporal Distribution of Rainfall Seasonality and Extreme Events Based on a 12-year TRMM Time Series. http://www.geog.ucsb.edu/~bodo/TRMM/ (submitted for publication).
Borchers, B., Marrero, S., Balco, G., Caffee, M., Goehring, B., Lifton, N., Nishiizumi, K., Phillips, F., Schaefer, J., Stone, J., 2016. Geological calibration of spallation production rates in the CRONUS-earth project. Quat. Geochronol. 31, 188–198.
Brown, E.T., Stallard, R.F., Larsen, M.C., Raisbeck, G.M., Yiou, F., 1995. Denudation rates determined from the accumulation of in situ-produced ^{10}Be in the Luquillo Experimental Forest, Puerto Rico. Earth Planet. Sci. Lett. 21, 125–139.
Brown, E.T., Stallard, R.F., Larsen, M.C., Bourlés, D.L., Raisbeck, G.M., Yiou, F., 1998. Determination of predevelopment denudation rates of an agricultural watershed (Cayaguás River, Puerto Rico) using in-situ produced ^{10}Be in river-borne quartz. Earth Planet. Sci. Lett. 160, 723–728.
Churches, C., Weber, J., Robertson, R., La Femina, P., Geirsson, H., Shaw, K., Higgins, M., Miller, K., 2014. New GPS evidence for continental transform fault creep, Central Range fault, Trinidad, and its geological and hazard implications. Geol. Soc. Am. Abstr. Prog. 46 (6), 360 (141-17).
Clark, S.A., Levander, A., Magnani, M.B., Zelt, C.A., 2008b. Negligible convergence and lithospheric tearing along the Caribbean–South American plate boundary at 64°W. Tectonics 27 (6), TC6013.
Clark, S.A., Sobiesiak, M., Zelt, C.A., Magnani, M.B., Miller, M.S., Bezada, M.J., Levander, A., 2008c. Identification and tectonic implications of a tear in the South American plate at the southern end of the Lesser Antilles. Geochem. Geophys. Geosyst. 9 (11), Q11004.
Clark, S.A., Zelt, C.A., Magnani, M.B., Levander, A., 2008a. Characterizing the Caribbean–South American plate boundary at 64°W using wide-angle seismic data. J. Geophys. Res. Solid Earth 113 (B07401).
Cruz, L., Fayon, A., Teyssier, C., Weber, J., 2007. Exhumation and deformation processes in transpressional orogens: the Venezuelan Paria Peninsula, SE Caribbean-South American plate boundary. In: Till, A.B., Roeske, S.M., Sample, J.C., Foster, D.A. (Eds.), Exhumation Associated With Continental Strike-Slip Systems. Geological Society of America Special Paper Vol. 434. pp. 149–165.
Cyr, A.J., Granger, D.E., Olivetti, V., Molin, P., 2010. Quantifying rock uplift rates using channel steepness and cosmogenic nuclide-determined erosion rates: examples from northern and southern Italy. Lithosphere 2 (3), 188–198.
Denison, C.W., 2008. Apatite Fission-track Thermochronology, Northern Range, Trinidad (and Paria Peninsula, Venezuela). Undergraduate Thesis McNair Scholars Journal 12(1). Grand Valley State University, MI, pp. 25–39.
Dortch, J.M., Owen, L.A., Caffee, M.W., Kamp, U., 2011. Catastrophic partial drainage of Pangong Tso, northern India and Tibet. Geomorphology 125 (1), 109–121.
Flinch, J.F., Rambaran, V., Ali, W., Lisa, V.D., Hernández, G., Rodrigues, K., Sams, R., 1999. Structure of the Gulf of Paria pull-apart basin (Eastern Venezuela-Trinidad). In: Mann, P. (Ed.), Sedimentary Basins of the World. 4. Elsevier, pp. 477–494.
Foland, K.A., Speed, R., Weber, J., 1992. Geochronologic studies of the hinterland of the Caribbean orogen of Venezuela and Trinidad. Geol. Soc. Am. Abstr. Programs 24 (7),

A148.
Frey, M., Saunders, J., Schwander, H., 1988. The mineralogy and metamorphic geology of low-grade metasediments, Northern Range, Trinidad. J. Geol. Soc. 145 (4), 563–575.
Garciacaro, E., Mann, P., Escalona, A., 2011. Regional structure and tectonic history of the obliquely colliding Columbus foreland basin, offshore Trinidad and Venezuela. Mar. Pet. Geol. 28 (1), 126–148.
Giorgis, S., Weber, J., Sanguinito, S., Beno, C., Metcalf, J., 2016. Thermochronology constraints on Miocene exhumation in the Central Range Mountains, Trinidad. Geol. Soc. Am. Bull. B31363-1.
Gonzalez, V.S., Bierman, P.R., Fernandes, N.F., Rood, D.H., 2016a. Long-term background denudation rates of southern and southeastern Brazilian watersheds estimated with cosmogenic ^{10}Be. Geomorphology 268, 54–63.
Gonzalez, V.S., Bierman, P.R., Nichols, K.K., Rood, D.H., 2016b. Long-term erosion rates of Panamanian drainage basins determined using in situ ^{10}Be. Geomorphology 275, 1–15.
Govers, R., Wortel, M.J.R., 2005. Lithosphere tearing at STEP faults; response to edges of subduction zones. Earth Planet. Sci. Lett. 236, 505–523.
Granger, D.E., Kirchner, J.W., Finkel, R., 1996. Spatially averaged long-term erosion rates measured from in situ-produced cosmogenic nuclides in alluvial sediment. J. Geol. 104 (3), 249–257.
Gudmundsdottir, M.H., Blisniuk, K., Ebert, Y., Levine, N.M., Rood, D.H., Wilson, A., Hilley, G.E., 2013. Restraining bend tectonics in the Santa Cruz Mountains, California, imaged using ^{10}Be concentrations in river sands. Geology 41 (8), 843–846.
van der Hammen, T., Hooghiemstra, H., 2000. Neogene and Quaternary history of vegetation, climate, and plant diversity in Amazonia. Quat. Sci. Rev. 19 (8), 725–742.
Haug, G.H., Hughen, K.A., Sigman, D.M., Peterson, L.C., Röhl, U., 2001. Southward migration of the intertropical convergence zone through the Holocene. Science 293, 1304–1308.
Helmer, E.H., Ruzycki, T.S., Benner, J., Voggesser, S.M., Scobie, B.P., Park, C., Fanning, D.W., Ramnarine, S., 2012. Detailed maps of tropical forest types are within reach: forest tree communities for Trinidad and Tobago mapped with multiseason Landsat and multiseason fine-resolution imagery. For. Ecol. Manag. 279, 147–166.
Hughen, K.A., Eglinton, T.I., Xu, L., Makou, M., 2004. Abrupt tropical vegetation response to rapid climate changes. Science 304, 1955–1959.
Insel, N., Ehlers, T.A., Schaller, M., Barnes, J.B., Tawackoli, S., Poulsen, C.J., 2010. Spatial and temporal variability in denudation across the Bolivian Andes from multiple geochronometers. Geomorphology 122, 65–77.
Istanbulluoglu, E., Bras, R.L., 2005. Vegetation-modulated landscape evolution: effects of vegetation on landscape processes, drainage density, and topography. J. Geophys. Res. 110, F02012. http://dx.doi.org/10.1029/2004JF000249.
Kohl, C.P., Nishiizumi, K., 1992. Chemical isolation of quartz for measurement of in-situ–produced cosmogenic nuclides. Geochim. Cosmochim. Acta 56 (9), 3583–3587.
Kooi, H., Beaumont, C., 1996. Large-scale geomorphology: classical concepts reconciled and integrated with contemporary ideas via a surface processes model. J. Geophys. Res. Solid Earth 101 (B2), 3361–3386.
Kugler, H.G., 1959. Geological Map and Sections of Trinidad. Petroleum Association of Trinidad, Port of Spain scale 1:100,000. (1 sheet).
Lal, D., 1991. Cosmic ray labeling of erosion surfaces: in situ nuclide production rates and erosion models. Earth Planet. Sci. Lett. 104 (2), 424–439.
Levander, A., Bezada, M.J., Niu, F., Humphreys, E.D., Palomeras, I., Thurner, S.M., Masy, J., Schmitz, M., Gallart, J., Carbonell, R., Miller, M.S., 2014. Subduction-driven recycling of continental margin lithosphere. Nature 515 (7526), 253–256.
Marshall, J.L., Russo, R.M., 2005. Relocated aftershocks of the March 10, 1988 Trinidad earthquake: normal faulting, slab detachment and extension at upper mantle depths. Tectonophysics 398 (3–4), 101–114.
Miller, M.S., Becker, T.W., 2012. Mantle flow deflected by interactions between subducted slabs and cratonic keels. Nat. Geosci. 5 (10), 726–730.
Miller, M.S., Levander, A., Niu, F., Li, A., 2009. Upper mantle structure beneath the Caribbean-South American plate boundary from surface wave tomography. J. Geophys. Res. Solid Earth 114 (B1), B01312.
Molnar, P., Sykes, L.R., 1969. Tectonics of the Caribbean and Middle America regions from focal mechanisms and seismicity. Geol. Soc. Am. Bull. 80, 1639–1684.
Morell, M., 2009. Quaternary Geology, Toco, Trinidad, West Indies. Undergraduate Thesis McNair Scholars Journal 13(1). Grand Valley State University, MI, pp. 84–103.
Nichols, K.K., Bierman, P., Finkel, R.C., Larsen, J., 2005. Long-term sediment generation rates for the Upper Río Chagres basin: evidence from cosmogenic ^{10}Be. In: Harmon, R.S. (Ed.), The Río Chagres, Panama: A Multidisciplinary Profile of a Tropical Watershed. Springer, The Netherlands, pp. 297–313.
Niemi, N.A., Oskin, M., Burbank, D.W., Heimsath, A.M., Gabet, E.J., 2005. Effects of bedrock landslides on cosmogenically determined erosion rates. Earth Planet. Sci. Lett. 237, 480–498.
Nishiizumi, K., Imamura, M., Caffee, M.W., Southon, J.R., Finkel, R.C., McAninch, J., 2007. Absolute calibration of ^{10}Be AMS standards. Nucl. Instrum. Methods Phys. Res., Sect. B 258 (2), 403–413.
Olen, S.M., Bookhagen, B., Strecker, M.R., 2016. Role of climate and vegetation density in modulating denudation rates in the Himalaya. Earth Planet. Sci. Lett. 445, 57–67.
Pazzaglia, F.J., Brandon, M.T., 1996. Macrogeomorphic evolution of the post-Triassic Appalachian mountains determined by deconvolution of the offshore basin sedimentary record. Basin Res. 8 (3), 255–278.
Pelletier, J.D., Barron-Gafford, G.A., Breshears, D.D., Brooks, P.D., Chorover, J., Durcik, M., Harman, C.J., Huxman, T.E., Lohse, K.A., Lybrand, R., Meixner, T., McIntosh, J.C., Papuga, S.A., Rasmussen, C., Schaap, M., Swetnam, T.L., Troch, P.A., 2013. Coevolution of nonlinear trends in vegetation, soils, and topography with elevation and slope aspect: a case study in the sky islands of southern Arizona. J. Geophys. Res. Earth Surf. 118 (2), 741–758.
Peltier, W.R., Fairbanks, R.G., 2006. Global glacial ice volume and Last Glacial Maximum duration from an extended Barbados sea level record. Quat. Sci. Rev. 25 (23–24), 3322–3337.
Peterson, L.C., Haug, G.H., Hughen, K.A., Röhl, U., 2000. Rapid changes in the hydrologic cycle of the tropical Atlantic during the Last Glacial. Science 290, 1947–1951.
Pindell, J.L., Higgs, R., Dewey, J.F., 1998. Cenozoic palinspastic reconstruction, paleogeographic evolution, and hydrocarbon setting of the northern margin of South America. In: Pindell, J.L., Drake, C.L. (Eds.), Paleogeographic Evolution and Non-glacial Eustasy, northern South America. SEPM (Society for Sedimentary Geology), Special Publication Vol. 58. pp. 45–86.
Portenga, E.W., Bierman, P.R., 2011. Understanding earth's eroding surface with ^{10}Be. GSA Today 21 (8), 4–10.
Portenga, E.W., Bierman, P.R., Duncan, C., Corbett, L.B., Kehrwald, N.M., Rood, D.H., 2015. Erosion rates of the Bhutanese Himalaya determined using in situ-produced ^{10}Be. Geomorphology 233, 112–126.
Prentice, C.S., Weber, J.C., Crosby, C.J., Ragona, D., 2010. Prehistoric earthquakes on the Caribbean–South American plate boundary, Central Range fault, Trinidad. Geology 38 (8), 675–678.
Pupim, F.D.N., Bierman, P.R., Assine, M.L., Rood, D.H., Silva, A., Merino, E.R., 2015. Erosion rates and landscape evolution of the lowlands of the Upper Paraguay river basin (Brazil) from cosmogenic ^{10}Be. Geomorphology 234, 151–160.
Ramcharan, E.K., 2004. Mid-to-late Holocene sea level influence on coastal wetland development in Trinidad. Quat. Int. 120 (1), 145–151.
Reiners, P.W., Zhou, Z., Ehlers, T.A., Xu, C., Brandon, M.T., Donelick, R.A., Nicolescu, S., 2003. Post-orogenic evolution of the Dabie Shan, eastern China, from (U–Th)/He and fission-track thermochronology. Am. J. Sci. 303, 489–518.
Riebe, C.S., Granger, D.E., 2013. Quantifying effects of deep and near-surface chemical erosion on cosmogenic nuclides in soils, saprolite, and sediment. Earth Surf. Process. Landf. 38 (5), 523–533.
Riebe, C.S., Kirchner, J.W., Finkel, R.C., 2003. Long-term rates of chemical weathering and physical erosion from cosmogenic nuclides and geochemical mass balance. Geochim. Cosmochim. Acta 67 (22), 4411–4427.
Ritter, J., Weber, J., 2007. In: Geomorphology and Quaternary Geology of the Northern Range, Trinidad and Paria Peninsula, Venezuela: Recording Quaternary Subsidence and Uplift Associated With a Pull-apart Basin. Proceedings, Geological Society of Trinidad and Tobago, Fourth Geological Conference.
Russo, R.M., Speed, R.C., 1992. Oblique collision and tectonic wedging of the South American continent and Caribbean terranes. Geology 20, 447–450.
Russo, R.M., Speed, R.C., 1994. Spectral analysis of gravity anomalies and the architecture of tectonic wedging, NE Venezuela and Trinidad. Tectonics 13 (3), 613–622.
Russo, R.M., Speed, R.C., Okal, E.A., Shepherd, J.B., Rowley, K.C., 1993. Seismicity and tectonics of the southeastern Caribbean. J. Geophys. Res. Solid Earth 98 (B8), 14299–14319.
Small, E.E., Anderson, R.S., 1998. Pleistocene relief production in Laramide mountain ranges, western United States. Geology 26 (2), 123–126.
Soto, D., Mann, P., Escalona, A., 2011. Miocene-to-recent structure and basinal architecture along the Central Range strike-slip fault zone, eastern offshore Trinidad. Mar. Pet. Geol. 28 (1), 212–234.
Speed, R.C., 1985. Cenozoic collision of the Lesser Antilles Arc and continental South America and the origin of the El Pilar fault. Tectonics 4 (1), 41–69.
Speed, R., Russo, R., Weber, J., Rowley, K.C., 1991. Evolution of Southern Caribbean Plate Boundary, vicinity of Trinidad and Tobago: discussion. Am. Assoc. Pet. Geol. Bull. 75 (11), 1789–1794.
Stone, J.O., 2000. Air pressure and cosmogenic isotope production. J. Geophys. Res. Solid Earth 105 (B10), 23753–23759.
Strahler, A.N., 1952. Hypsometric (area-altitude) analysis of erosional topography. Geol. Soc. Am. Bull. 63 (11), 1117–1142.
Turcotte, D.L., Schubert, G., 2014. Geodynamics. Cambridge University Press.
Vanacker, V., von Blanckenburg, F., Govers, G., Molina, A., Poesen, J., Deckers, J., Kubik, P., 2007. Restoring dense vegetation can slow mountain erosion to near natural benchmark levels. Geology 35 (4), 303–306.
VanDecar, J.C., Russo, R.M., James, D.E., Ambeh, W.B., Franke, M., 2003. Aseismic continuation of the Lesser Antilles slab beneath continental South America. J. Geophys. Res. Solid Earth 108 (B1), 2043.
de Verteuil, L., Ramlal, B., Weber, J., 2006. Trinidad Geological GIS–Module 1–Surface Geology and Geography. Latinum Ltd., Port-of-Spain, Trinidad.
Weber, J.C., 2005. Neotectonics in the Trinidad and Tobago, West Indies segment of the Caribbean–South American plate boundary. Geol. Inst. Hung. 204 (Occasional Papers), 21–29.
Weber, J.C., Dixon, T.H., DeMets, C., Ambeh, W.B., Jansma, P., Mattioli, G., Saleh, J., Sella, G., Bilham, R., Pérez, O.J., 2001a. GPS estimate of relative motion between the Caribbean and South American plates, and geologic implications for Trinidad and Venezuela. Geology 29 (1), 75–78.
Weber, J.C., Ferrill, D.A., Roden-Tice, M.K., 2001b. Calcite and quartz microstructural geothermometry of low-grade metasedimentary rocks, Northern Range, Trinidad. J. Struct. Geol. 23 (1), 93–112.
Weber, J.C., Saleh, J., Balkaransingh, S., Dixon, T., Ambeh, W., Leong, T., Rodriguez, A., Miller, K., 2011. Triangulation-to-GPS and GPS-to-GPS geodesy in Trinidad, West Indies: neotectonics, seismic risk, and geologic implications. Mar. Pet. Geol. 28 (1), 200–211.
Wesnousky, S.G., Aranguren, R., Rengifo, M., Owen, L.A., Caffee, M.W., Murari, M.K., Pérez, O.J., 2012. Toward quantifying geomorphic rates of crustal displacement, landscape development, and the age of glaciation in the Venezuelan Andes. Geomorphology 141–142, 99–113.
White, A.F., Blum, A.E., Schulz, M.S., Vivit, D.V., Stonestrom, D.A., Larsen, M., Murphy, S.F., Eberl, D., 1998. Chemical weathering in a tropical watershed, Luquillo mountains, Puerto Rico: I. Long-term versus short-term weathering fluxes. Geochim.

Cosmochim. Acta 62 (2), 209–226.
Willett, S.D., Brandon, M.T., 2002. On steady states in mountain belts. Geology 30 (2), 175–178.
Wittmann, H., von Blanckenburg, F., Guyot, J.L., Maurice, L., Kubik, P.W., 2009. From source to sink: preserving the cosmogenic ^{10}Be-derived denudation rate signal of the Bolivian Andes in sediment of the Beni and Mamoré foreland basins. Earth Planet. Sci. Lett. 288 (3–4), 463–474.
Wittmann, H., von Blanckenburg, F., Maurice, L., Guyot, J.-L., Filizola, N., Kubik, P.W., 2011. Sediment production and delivery in the Amazon River basin quantified by in situ–produced cosmogenic nuclides and recent river loads. Geol. Soc. Am. Bull. 123 (5–6), 934–950.
Wobus, C.W., Tucker, G.E., Anderson, R.S., 2010. Does climate change create distinctive patterns of landscape incision? J. Geophys. Res. Earth Surf. 115, F04008.
WRA (Trinidad and Tobago Water Resources Agency), 2001. Integrating the Management of Watersheds and Coastal Areas in Trinidad and Tobago. (Prepared by the Water Resource Agency for the Ministry of the Environment, Complex Independent Square, Port of Spain).
Yanites, B.J., Tucker, G.E., Anderson, R.S., 2009. Numerical and analytical models of cosmogenic radionuclide dynamics in landslide-dominated drainage basins. J. Geophys. Res. 114 (F1), F01007.